Microstructural evolution of three potential fusion candidate steels under ion-irradiation

[1]N. Zimber, [1]P. Vladimirov, [1]M. Klimenkov, [1]U. Jäntsch, [2]R. Vila, [1]V. Chakin, [2]F. Mota

[1]Karlsruhe Institute of Technology (KIT), Institute for Applied Materials – Applied Materials Physics (IAM-AWP), Herman-von-Helmholtz-Platz 1, 76344 Eggenstein-Leopoldshafen, Germany

[2]National Fusion Laboratory-Fusion Materials, CIEMAT, 28040, Madrid, Spain

Corresponding author: Nikolai Zimber

Address: Karlsruhe Institute of Technology (KIT), Institute for Applied Materials – Applied Materials Physics (IAM-AWP), Herman-von-Helmholtz-Platz 1, 76344 Eggenstein-Leopoldshafen, Germany

Telephone number: +49 721 608 28540

E-mail address: nikolai.zimber@kit.edu

Keywords: EELS, Ion implantation, EUROFER97, ODS, ferritic ODS, helium, hydrogen,

Graphical Abstract

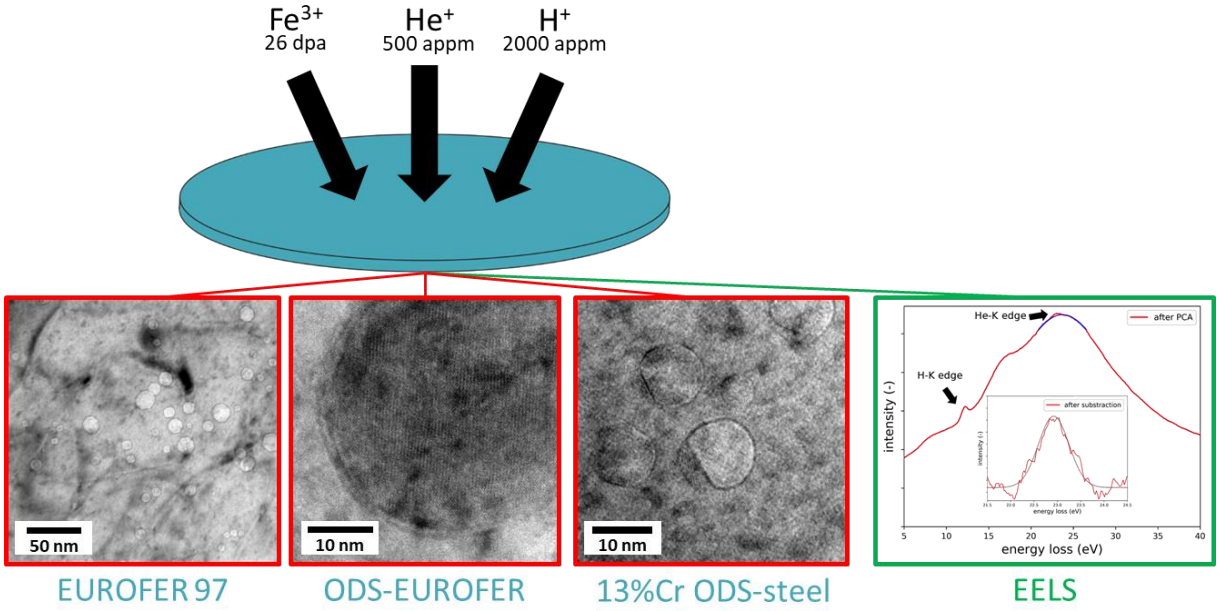

Abstract

The present paper studies the gas bubble distribution in triple beam irradiated (Fe^+, He^+, H^+) EUROFER97, ODS-EUROFER and a 13%Cr ODS-steel. All materials were irradiated 350 °C, 450 °C and 550 °C up to a displacement damage of 40 dpa, a helium concentration of ~12.5 appm He/dpa and a final hydrogen content of ~50 appm H/dpa, respectively.

While most of the bubbles, with diameters up to 107 nm, in the 13%Cr ODS-steel were found to be attached to the ODS-particles at all temperatures, they showed a homogenous distribution in EUROFER97 at 350 °C. At 450 °C however, many small clusters with mainly facetted cavities were observed, whereas at 550 °C most of the bubbles were localized at microstructural sinks like grain boundaries, dislocations or precipitates. The largest bubble found in EUROFER97 had a diameter of ~19 nm.

In both materials, the largest bubbles were located in the area where, according to SRIM calculations, superposition of maximum displacement damage and highest gas concentration occurred. This observation suggests that synergetic effects between helium and hydrogen strongly influenced the bubble growth but not the bubble nucleation.

Despite exhaustive analysis, no bubbles could be identified in any of the three ODS-EUROFER lamellae. Apparently, bubbles have formed only below the TEM resolution limit or the helium was evenly distributed within the grains or at the particle-matrix interface.

In addition, electron energy loss spectroscopy (EELS) was used to confirm the existence of helium and hydrogen inside closed gas bubbles.

1. Introduction

Due to the neutron radiation inside future fusion reactors, helium and hydrogen are formed in the structural components of future fusion reactors as a result of transmutation processes and have a lasting influence on its mechanical properties [1–5]. The formation of nanometer-sized helium bubbles leads to successive embrittlement and swelling of the structural materials [6–9]. For this reason, the prediction and mitigation of radiation-induced gas bubble formation is one of the most important challenges on the way to fusion energy. In order to estimate the consequences of the superposition of displacement damage and continuous gas production, the validation of materials under realistic scenarios is essential. Currently, there is no research facility available in which the exact fusion conditions can be simulated. Therefore presently other methods [5,10–12] must be used to test the material behaviour in future fusion power plants. Ion implantation using single, dual or triple beams is a promising alternative for obtaining information about the ageing behavior of materials under fusion conditions within a very short time. [13]

In this study, the microstructural changes resulting from irradiation-induced helium and hydrogen production in combination with displacement damage are investigated in potential structural materials for fusion technology. Therefore, the low-activating ferritic/martensitic (F/M) steels EUROFER97, ODS-EUROFER as well as a ferritic 13%Cr ODS-steel (HIP-ODS) were irradiated with a triple ion beam (Fe^{3+}, He^{+}, H^{+}) at 350 °C, 450 °C and 550 °C up to 40 dpa, 500 appm He and 2000 appm H, respectively. Afterwards, the gas bubble distribution (number, size, distribution and morphology) was analyzed in the transmission electron microscope (TEM).

2. Experimental Procedure

2.1 Materials

In this work EUROFER97, ODS-EUROFER and a ferritic 13%Cr ODS-steel were investigated. Chemical composition of all three materials can be seen in Table 1.

Table 1: Chemical composition of EUROFER97 [14], ODS-EUROFER and the 13%Cr ODS-steel

element (weight. %)	EUROFER97	ODS-EUROFER	13%Cr ODS-steel
C	0.12	0.071	0.0562
Cr	8.91	8.92	12.97
W	1.08	1.11	1.82
Mn	0.48	0.408	0,0308
V	0.2	0.193	0.0532
Ta	0.14	0.081	< 0.001
N	0.02	0.0278	0.0270
Si	0.04	0.111	0.0467
Y	-	0.192	0.2077
O	-	0.144	0.0468
Fe	balance	balance	balance

The EUROFER97 samples originate from batch E83697 and were manufactured by Böhler Austria GmbH. Prior to the irradiation, the samples were austinitized for 30 minutes at 980 °C, quenched in air and then tempered for 2 h at 760 °C. The ODS-EUROFER samples were produced by mechanical alloying of EUROFER powder with 0.3 % yttrium at Plansee GmbH. After hot isostatic pressing (HIP), this material was rolled, austinitized at 1100 °C for 30 min and then tempered at 750 °C for 2 h. The ferritic 13%Cr ODS-steel was produced at the Institute

of Applied Materials – Applied Materials Physics (IAM-AWP) of the Karlsruhe Institute of Technology (KIT) and was exclusively HIPt at 1100 °C and received no additional heat treatment. Quantitative TEM-analysis of the two ODS-steels was already performed in an earlier study [15]. The results are presented in Table 2. Mixing of the alloying elements for the ODS-steels was partly done in glove boxes under Ar-atmosphere.

Table 2: Results of the quantitative analysis of ODS-EUROFER and 13%Cr ODS-steel. [15]

	ODS-EUROFER	13%Cr ODS-steel
ferritic grain size (μm)	4-7	6-8
martensitic grain size (μm)	-	0.4-0.8
carbid size (nm)	50-800	-
oxide average size (nm)	11±6	10±3
oxide number density (m^{-3})	5×10^{21}	8×10^{21}
Dislocation number density (m^{-3})	10^{8}	10^{8}

2.2 Triple ion-beam irradiation

Discs with a diameter of 3 mm were prepared from all three materials and then irradiated with a triple ion-beam at the Joint Accelerator for Nanoscience and Nuclear Simulation (JANNuS) at the Université Paris-Sud, Saclay at 350 °C, 450 °C and 550 °C. This temperature range limits the range of application of EUROFER97. Below 350 °C the material undergoes severe embrittlement [16], above 550 °C creep becomes a critical factor [17].

All relevant experimental parameters for the irradiation (see Table 2) were calculated using the full cascade mode in SRIM [18] assuming a threshold energy of 40 eV for the Fe atom displacement. The He- and H-ion concentrations as well as the displacement damage reached its maximum over the depth range from 1 to 2 μm. The goal was to obtain the flattest possible implantation profile at the desired depth by successive implantation of the ions at different energies using beam degraders. More detailed information about the irradiation conditions as well as the implantation profile can be found in [19].

Table 3: Irradiation parameters for the triple beam irradiation of the three steels

ion	energy	temperature (°C)	dose (ion cm^{-2} s^{-1})	fluence (ion cm^{-2})	dose (dpa)/ concentration (appm)
Fe^{3+}	10 MeV		1.71×10^{12}	4.3×10^{16}	40 dpa
He^{+}	1.3 MeV	350/450/550	2.30×10^{11}	5.8×10^{15}	500 appm
H^{+}	600 keV		7.14×10^{11}	1.80×10^{16}	2000 appm

2.3 Microstructural investigations & analytical TEM

TEM lamellae of all three materials with sizes between 6-7 µm were prepared using a Zeiss NVision FIB microscope equipped with a Ga^{+} liquid-metal ion source. All foils were taken from the inner third of the "bulk" samples, since the radiation should have had its full effect here. Afterwards all lamellae were systematically examined from the surface until the end of the lamellae using a FEI Tecani 20 equipped with a field emission gun (FEG) operated at 200 kV.

By definition, bubbles are gas-filled cavities. However, within the scope of this work we did not verify for all materials weather helium or hydrogen resides inside the defect cluster. For the sake of simplicity, all defects, whether they are bubbles or just cavities, will be referred to as bubbles, even if no gas might be present in the defect cluster. In order to distinguish the bubbles in the TEM from other microstructural defects, or to make them visible at all, it is necessary to take images outside the focal plane. At the transition from upper to lower focus, the contrast of the bubbles changes from a black dot with a white fresnel fringe to a white dot with a black fresnel fringe. [20,21]

In order to confirm the existence of helium and hydrogen inside the defect clusters, electron energy loss spectroscopy (EELS) measurements of all three materials were performed using a FEI Talos equipped with a x-FEG. For the spectrum image (SI) acquisition the microscope was operated at 200 kV using a Dual EELS-Gatan Imaging Filter (GIF) Infinium. The obtained energy resolution was 0.95 eV with a camera length of 37 mm. The dispersion was set to 0.025 eV/channel.

2.4 Statistical Characteristics

The analysis of the gas bubble distribution was done with the image processing package Fiji [22]. In order to ensure uniform results, the statistical values such as bubble number and size were measured in a 175 nm x 175 nm window for each depth. The FIB preparation partially damaged the surfaces of the lamellae. In order to obtain comparable results from all samples and temperatures the statistical evaluation therefore started at a depth of 500 nm. According to ASTM E521-96 [23] the bubbles can be assumed to be completely spherical. The size is thus determined simply by the diameter and the volume V is given by $V = \frac{4}{3} r^3 \pi$, where r is the bubble radius. The swelling $\frac{\Delta V}{V_0}$ can be calculated as $\frac{\Delta V}{V_0} = 100 \text{ x } \left[\frac{\Delta V}{V_t - \Delta V}\right]$. Here ΔV is the volume of all bubbles measured in a total volume V_t. The initial volume V_0 is equal to $V_t - \Delta V$. One has to keep in mind, that the calculated swelling only considers bubbles that are visible in TEM. However, bubbles with a diameter of < 0.5 nm should only have a minor influence on the swelling behaviour.

Finally, the bubble density ρ is calculated as $\rho = \left(\frac{1}{At}\right) \sum^i N_i$, where A is the area where the bubbles have been measured, t the average thickness in that area and N_i the number of bubbles measured. The foil thickness of each lamella was determined by EELS using the log-ratio technique [24].

3. Experimental Results

3.1 EUROFER 97

350°C

After irradiation at 350 °C the EUROFER97 sample predominantly showed bubbles with a diameter of ~1 nm. All bubbles had a round geometry and were evenly distributed in the matrix over the entire sample. In the range between 0.5 µm and 1.5 µm, bubbles with diameters of up to ~2.4 nm could also be found sporadically. The typical microstructure can bee seen in Figure 1 (left).

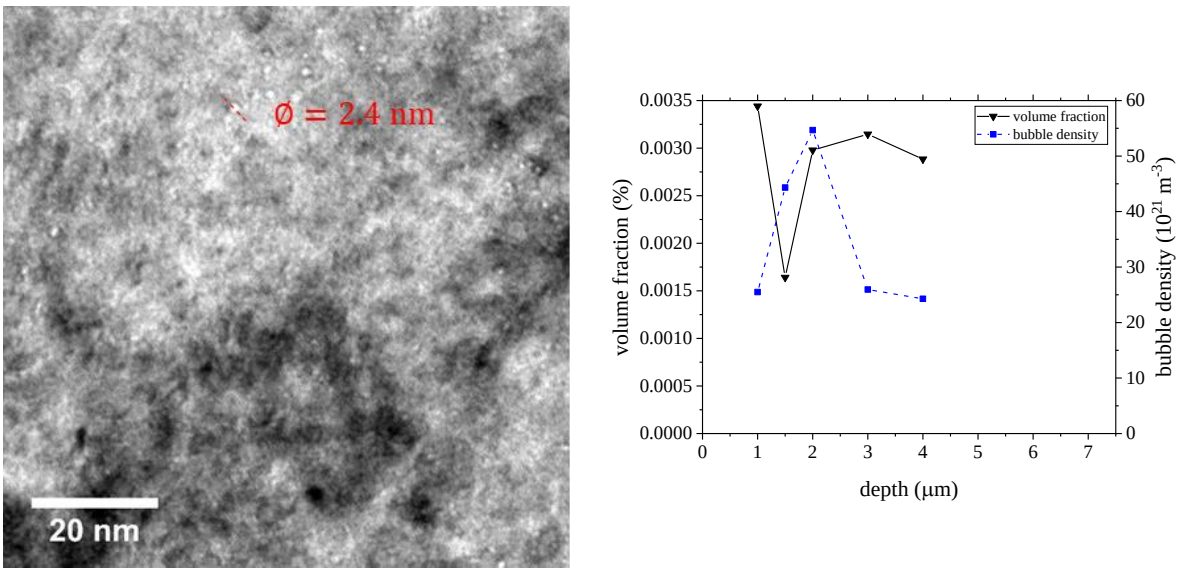

Figure 1: (left) Gas bubble distribution close to the surface and (right) volume fraction of the bubbles and bubble density for the EUROFER97 irradiated at 350 °C up to 40 dpa, 12.5 appm He/dpa and 50 appm H/dpa

In general, the distribution of gas bubbles at this temperature depends strongly on the depth (see Figure 1 (right)). Up to 2 µm, the number of bubbles increases sharply, then decreases rapidly. The same applies to the bubble density, which rises in the range between 1.5 µm and 2 µm up to 5.5 x 10^{22} m^{-3} and then drops significantly again. At this temperature the swelling is negligible. The maximum value is only ~0.0035 %. Starting from ~3.5 µm either no more bubbles have formed or they could no longer be resolved in the TEM.

450°C

The distribution of bubbles in irradiated at 450 °C EUROFER97 is completely different from that at 350 °C. The bubbles are no longer evenly distributed and both, round and polyhedral faceted geometries were formed. Most of the faceted bubbles are hexagonal, some are squared. Figure 2 shows a section of the investigated TEM lamella from the surface covered with platinum up to a depth of ~3000 nm. It can be clearly seen, that between 1500 nm and 2000 nm a large number of bubbles have formed. From ~2400 nm on no more bubbles could be observed or they were again too small to be resolved in the TEM. The mean bubble diameter was determined to be 2.6 nm at this temperature.

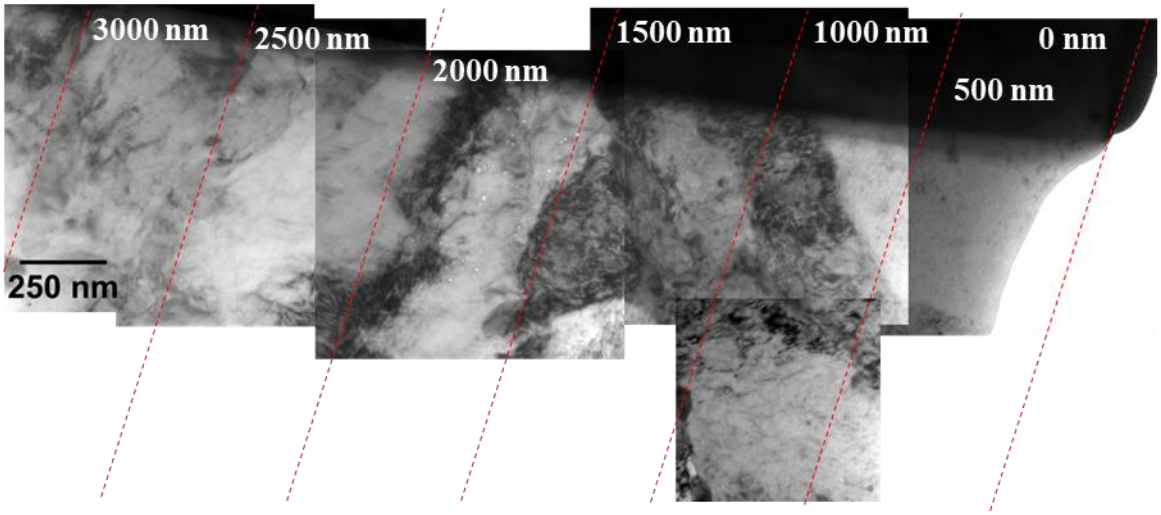

Figure 2: Section of the TEM lamella from the EUROFER97 sample irradiated at 450 °C up to 40 dpa, 12.5 appm He/dpa and 50 appm H/dpa. Most bubbles were found in a depth between 1500-2000 nm. At ~2.4 µm no more bubbles could be detected.

Figure 3 (right) shows the volume fraction and the bubble density as a function of the depth. In this sample bubbles with sizes from 1.2 nm to 19.3 nm were detected. As shown in Figure 3 (right), the largest bubble diameters were found at a depth between 1500 nm and 2000 nm. Figure 3 (left) shows how larger bubbles are often surrounded by much smaller ones. On the other hand, some bubbles overlap and seem to merge. Up to this depth, the bubbles were almost exclusively round. At greater depths, they also showed a clearly faceted structure and were repeatedly distributed in the matrix in the form of smaller clusters. Both the bubble density and the volume fraction of the bubbles, as well as the bubble size, have increased significantly between 1500 nm and 2000 nm. The sample has swollen by ~0.5 % in this area and has a bubble density of 1.5×10^{22} m^{-3}. From 2000 nm on, the bubble density has increased again to 2.2×10^{22} m^{-3} while the volume fraction has clearly decreased.

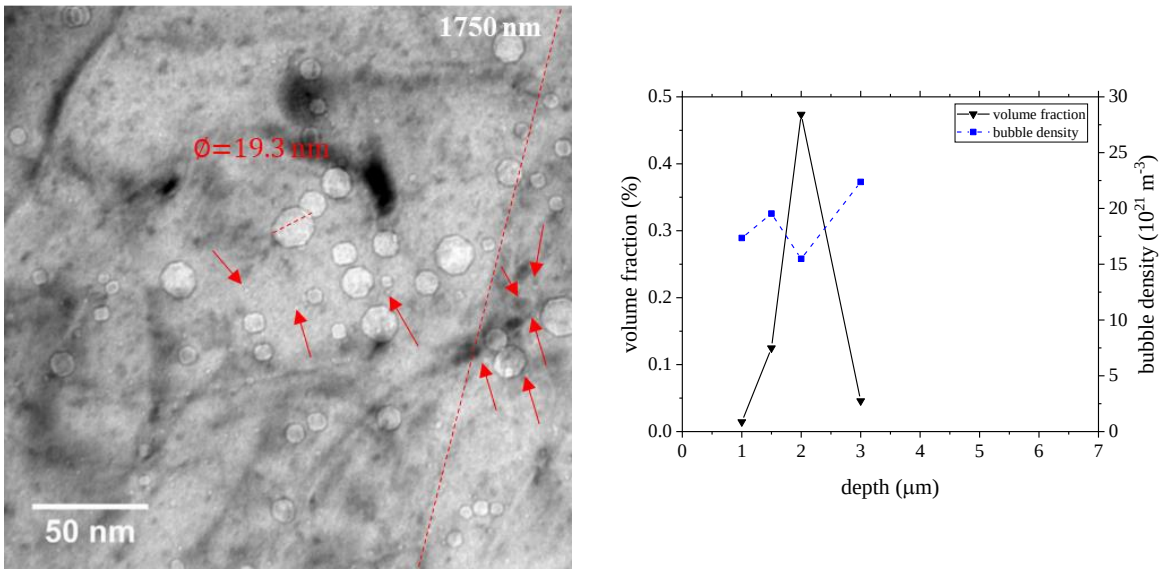

Figure 3: (left) Micrograph from the implantation region showing clusters of large and small bubbles and (right) volume fraction and bubble density of the EUROFER97 sample irradiated at 450 °C up to 40 dpa, 12.5 appm He/dpa and 50 appm H/dpa

550 °C

Investigation of the 550 °C sample revealed, that the vast majority of the bubbles have a round shape and are now also attached to lattice defects, especially in the implantation area between 1 µm and 2 µm. The few faceted bubbles have the same hexagonal structure as in the 450 °C sample. However, in the range up to ~200 nm no bubbles could be detected at this temperature. Between 250 nm and 1500 nm some small bubbles could be observed inside the grains. The average size in this area was determined to be ~3 nm.

As at 450 °C, the largest bubbles could be observed in an area between 1500 nm and 2000 nm. However, the maximum bubble size in this region is only 8.6 nm, and the maximum swelling value only 0.14 % (see Figure 4 (right)). From Figure 4 (left) it can be seen, that at a depth of 1-2 µm, the bubbles have nucleated mainly at microstructural sinks such as dislocation lines (1) and even more at grain boundaries (2). Also, bubbles had repeatedly attached themselves to precipitates, as shown in Figure 5.

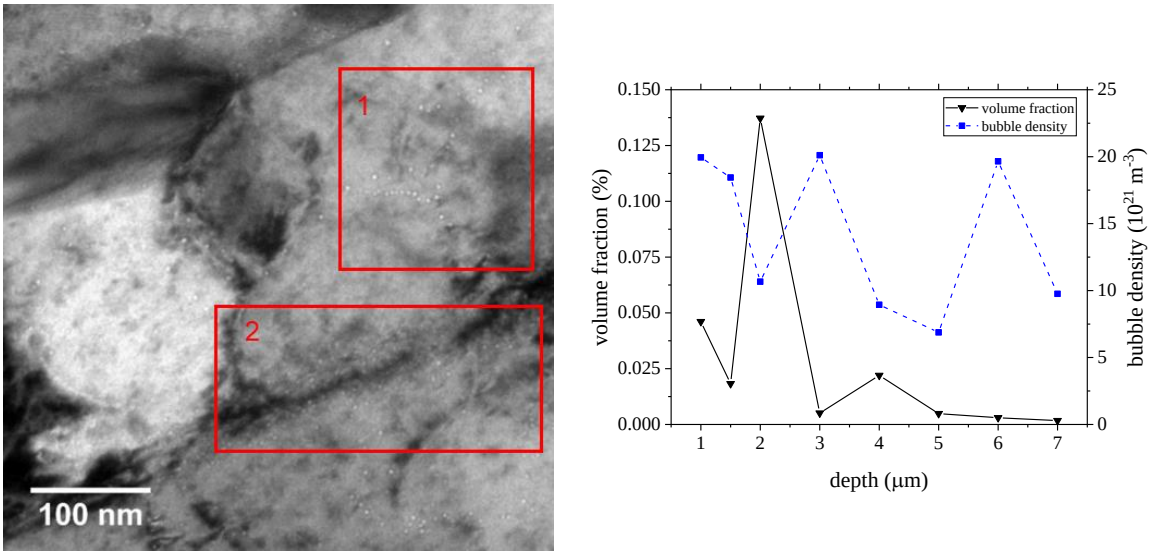

Figure 4: (left) Micrograph from the implantation region showing bubbles attached to (1) dislocation lines and (2) a grain boundary, (right) volume fraction and bubble density of the EUROFER97 sample irradiated at 550 °C up to 40 dpa, 12.5 appm He/dpa and 50 appm H/dpa

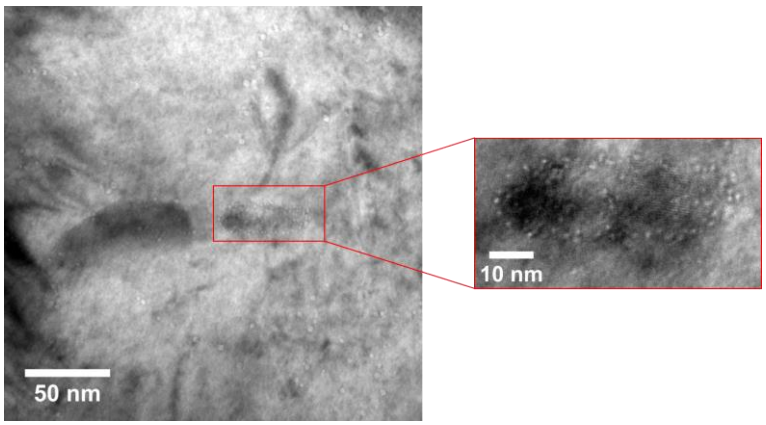

Figure 5: TEM image at a depth of about 1 µm. Clearly visible accumulation of bubbles at a carbide precipitation. The bubble density in the enlarged area is 6.0 x 10^{23} m^{-3}.

3.2 ODS-EUROFER

First TEM investigations of the ODS-EUROFER samples initially gave the impression, that small bubbles had formed at the surface of the ODS-particles in many places at all three irradiation temperatures. Figure 7 shows images from the implantation regions for the different temperatures. The red arrows mark structures that initially seem to be bubbles. On closer inspection in the high resolution transmission electron microscope (HRTEM) and by tilting the sample, however, it turned out that these features were almost always either small ODS-particles or simply contrast phenomena that looked like bubbles. Figure 6 (left) and (right) show how small ODS-particles with diameters of 2-4 nm are attached to much larger ones

7 shows the same typical structure for all three temperatures. Many ODS-particles, but no bubbles. Observation of all samples under different diffraction conditions remained unsuccessful as well.

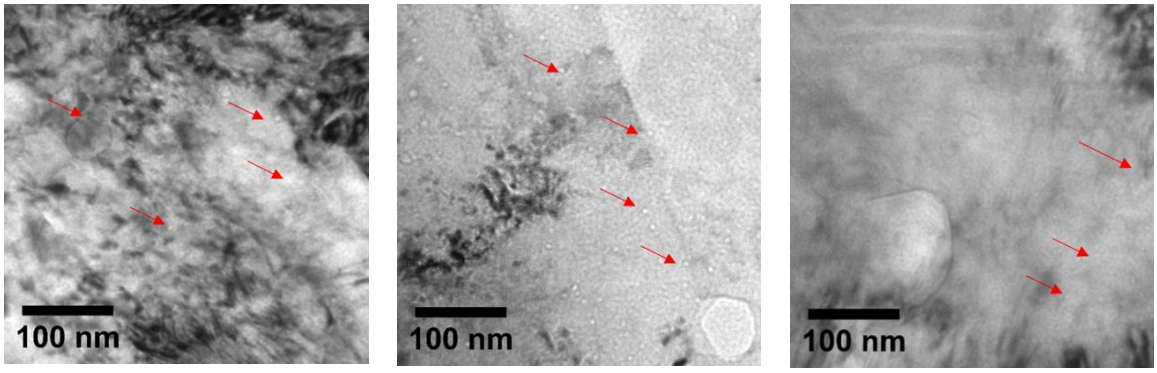

Figure 7: TEM micrographs taken from the ODS-EUROFER sample irradiated at (left) 350 °C, (middle) 450 °C and (right) 550 °C. The red arrows mark features that look like bubbles.

3.3 13%Cr-ODS steel

350 °C

The HIP-ODS sample irradiated at 350 °C revealed clearly visible bubbles already in the low magnification mode. Figure 8 also clearly shows, that the largest bubbles again formed between 1.5 µm and 2 µm and that bubbles could still be observed at a depth of ~4.2 µm. Up to ~1.2 µm it was sometimes very difficult to clearly identify bubbles as such. In this area, they were often smaller than 1.0 nm and could therefore not always be clearly distinguished from the image noise of the TEM, even in high resolution. However, there were also a few larger bubbles with a diameter of up to 10 nm in this range. From a depth of ~1.5 µm a clear jump in the bubble size and consequently also in the swelling could be observed (see Figure 9 (right)). In the area between 1.5-2 µm several bubbles with a size between 30-70 nm were formed and also the largest bubble with a diameter of ~107 nm was measured here. This resulted in a swelling of ~27 % in this area.

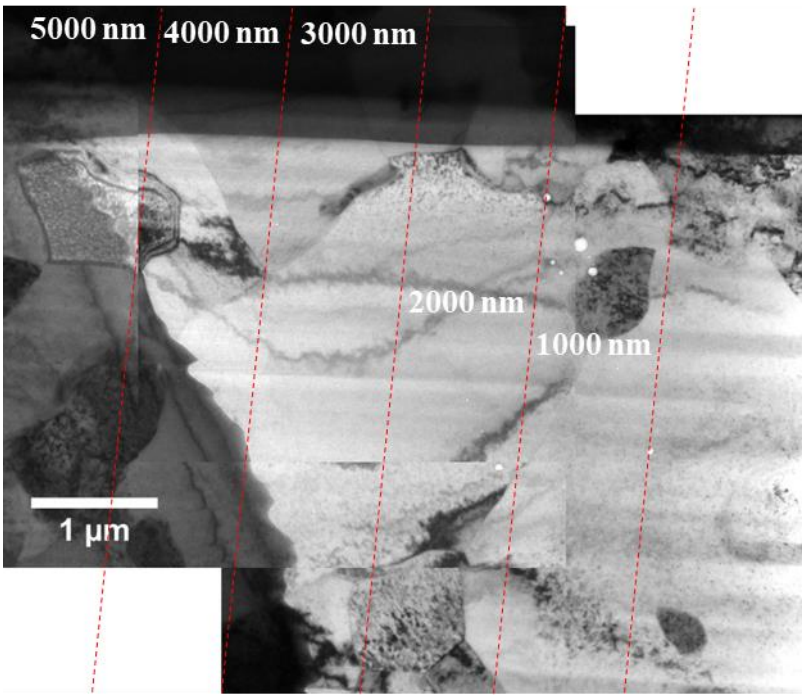

Figure 7: Section of the TEM lamella from the HIP-ODS sample which was irradiated at 350 °C up to 40 dpa, ~12.5 appm He/dpa and ~50 appm H/dpa. The largest bubbles were found in the range between 1500-2000 nm.

It is also noteworthy that all bubbles > 40 nm were apparently attached to half elliptical ODS-particles. In general, at this temperature, the majority of all visible bubbles, ~72 %, was formed at ODS-particles that were freely deposited in the matrix or at grain and phase boundaries. Only ~28 % were free inside the grain or not visibly attached to particles. At dislocation lines, directly at precipitates or grain boundaries no bubbles could be observed. With a few exceptions, all bubbles were spherical. Especially those that were visibly attached to ODS-particles. Only a few weakly faceted bubbles as shown in Figure 9 appeared. From a depth of 2 µm up to ~4.2 µm, a bubble distribution as shown in Figure 9 was observed throughout. At many places in the material, helium and vacancies accumulated at the surface of the ODS-particles. With increasing depth, the maximum bubble size has decreased while the number of smaller bubbles has increased. As a result, the bubble density between 3 µm and 4 µm initially increased up to 8.8×10^{21} m^{-3} before dropping down to 1.1×10^{21} m^{-3} at a depth of 5 µm.

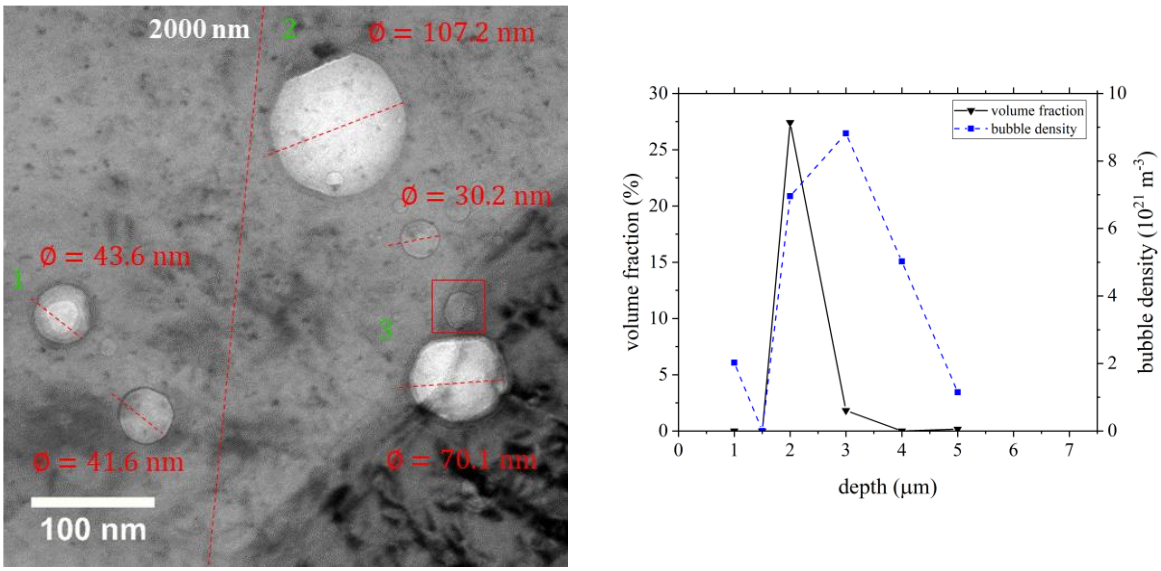

Figure 9: (left) Bubble distribution at a depth of ~2 µm in the HIP-ODS sample irradiated at 350 °C, the red area marks a weakly faceted bubble, bubbles 1-3 are clearly oxidized; (right) volume fraction of the bubbles and bubble density for the HIP-ODS irradiated at 350 °C up to 40 dpa, 12.5 appm He/dpa and 50 appm H/dpa

450 °C

In the 450 °C sample, considerably more bubbles than at 350 °C were detected. Up to a depth of ~6.5 nm, there were many small bubbles with diameters between 1.5 nm and 6 nm as well as individual larger bubbles with diameters up to ~70 nm (see Figure 10). Between 0.5 µm and 1 µm bubbles had already a size of up to 10 nm. The vast majority was attached to ODS-particles at this depth. In total, ~60 % of all bubbles were visibly attached to precipitates, grain boundaries or phase boundaries, ~15 % apparently to dislocation lines, the remaining 25 % were free in the matrix or not visibly attached to microstructural sinks.

From ~1.5 µm on the bubble distribution has changed significantly. The bubbles were no longer evenly distributed and the size distribution also showed a different picture than before. Individual, very large bubbles were now again and again linearly arranged together with many small bubbles, as can be seen in Figure 11. However, clearly visible dislocation lines or grain boundaries could not be observed at these locations under the given TEM operating conditions. In addition, it was sometimes relatively difficult to clearly identify the ODS-particles. At a depth of ~1.6 µm, the largest bubble with a diameter of 70.1 nm formed on an ODS-particle at 450 °C. As at 350 °C, smaller bubbles with diameters of up to ~8 nm were found exclusively on round ODS-particles. Usually, only a single bubble was visible on an ODS-particle. At this temperature, most of the bubbles were spherical, as shown in Figure 11. Especially the few larger bubbles with a diameter of ~18 nm were slightly faceted. The maximum swelling,

~7.1 %, was reached again between 1.5-2 µm. Since the entire helium was distributed over a few bubbles, two additional swelling maxima between 3-4 µm and 6-7 µm appeared. With 2.5 % and 4.6 %, however, they were smaller than the first one. It is also noteworthy that at all points where the sample is visibly swollen, the bubble density has decreased significantly each time.

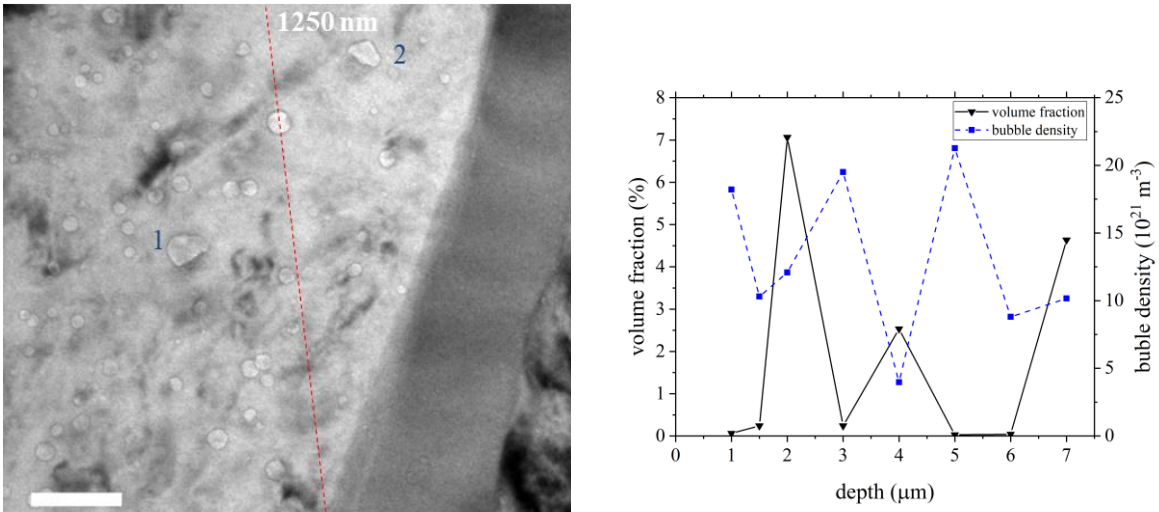

Figure 9: (left) Bubble distribution in ~1.2 µm depth with different bubble geometries(1: semicircular, 2: "conical") at the surface of ODS-particles; (right) volume fraction of the bubbles and bubble density for the HIP-ODS irradiated at 450 °C up to 40 dpa, 12.5 appm He/dpa and 50 appm H/dpa

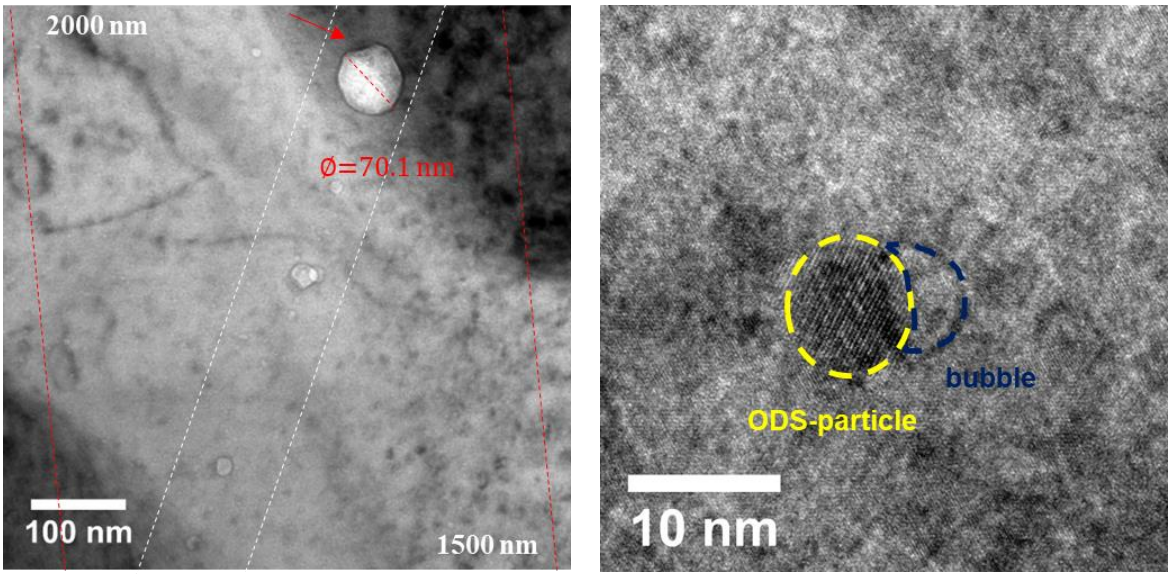

Figure 10: (left) TEM image of the 450 °C HIP-ODS sample in the range between 1500-2000 nm with linear arrangement of the bubbles marked by the white lines. The red arrow marks the precipitation to which the 70.1 nm sized bubble is attached. (right) HRTEM image of an ODS-particle with an attached bubble.

550 °C

After irradiation at 550 °C fewer bubbles and in the majority, smaller bubbles were formed compared to the irradiation at 450 °C. In addition, the bubbles were only visible up to a depth of ~3.8 µm. As with the two lower temperatures, a large bubble, with a diameter of 88.8 nm (see Figure 12), was formed between 1.5 µm and 2 µm, but it was smaller than the largest bubble at 350 °C. Furthermore, this bubble appears to have formed freely in the matrix. Between 1.5 µm and 3 µm, a linear arrangement of individual larger bubbles with several small bubbles, which usually had a size between 1.5 nm and 4 nm, could be observed again and again. In this range the bubble density increased from 9.1 x 10^{21} m^{-3} to 2.5 x 10^{22} m^{-3}. While the swelling increased in several places for the 450 °C sample, the swelling curve for this temperature shows only one maximum between 1.5 µm and 2 µm with a value of ~12.0 %. From ~2 µm on a significant increase in the number of bubbles was once again observed, before from ~3 µm on fewer bubbles were visible (see Figure 12 (right)). Some areas showed again linear alignments of bubbles as it can be seen from Figure 12 (left). Just as at 450 °C, ~60 % of the bubbles were attached to particles, ~25 % were freely distributed in the matrix or not recognizably attached to defects, and ~15 % were possibly attached to dislocation lines. Figure 12 also demonstrates that even at this temperature larger bubbles showed a slight faceting.

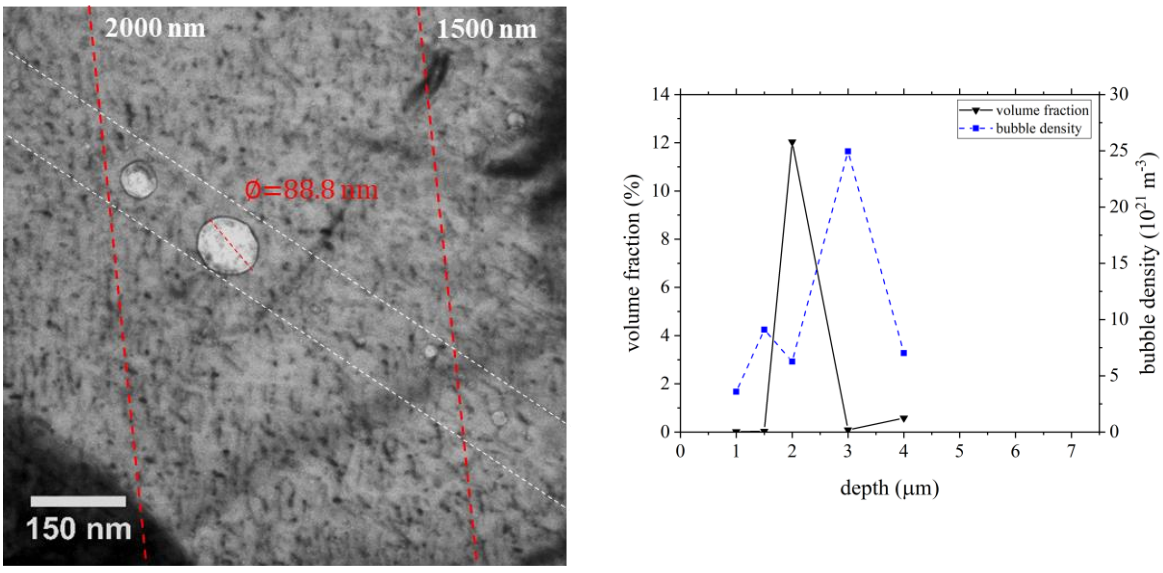

Figure 11: (left) Bubble distribution at 550 °C for the HIP-ODS sample, with a linear arrangement in the white marked area; (right) volume fraction of the bubbles and bubble density for the HIP-ODS irradiated at 550 °C up to 40 dpa, 12.5 appm He/dpa and 50 appm H/dpa

3.4 Analytical Transmission Electron Microscopy

EELS measurements were performed with all three materials aiming for the detection of hydrogen and helium within closed bubbles. As expected, we could not measure a signal for hydrogen or helium within ODS-EUROFER. We also looked for unusual changes in the elemental concentrations at the particle-matrix interfaces, that might be caused by voids or gas bubbles [25] but remained unsuccessful. Surprisingly, we also found no signs of helium and hydrogen in the EUROFER97 samples even though some bubbles had a size of up to 19 nm. Either our samples were still too thick for the detection of the two gases – t/λ was measured to be between 0.7-1 – or the gas concentration in single bubbles was just too low and below the detection limit of our microscope. The HIP-ODS samples, however, showed several bubbles with clear hydrogen and helium signatures.

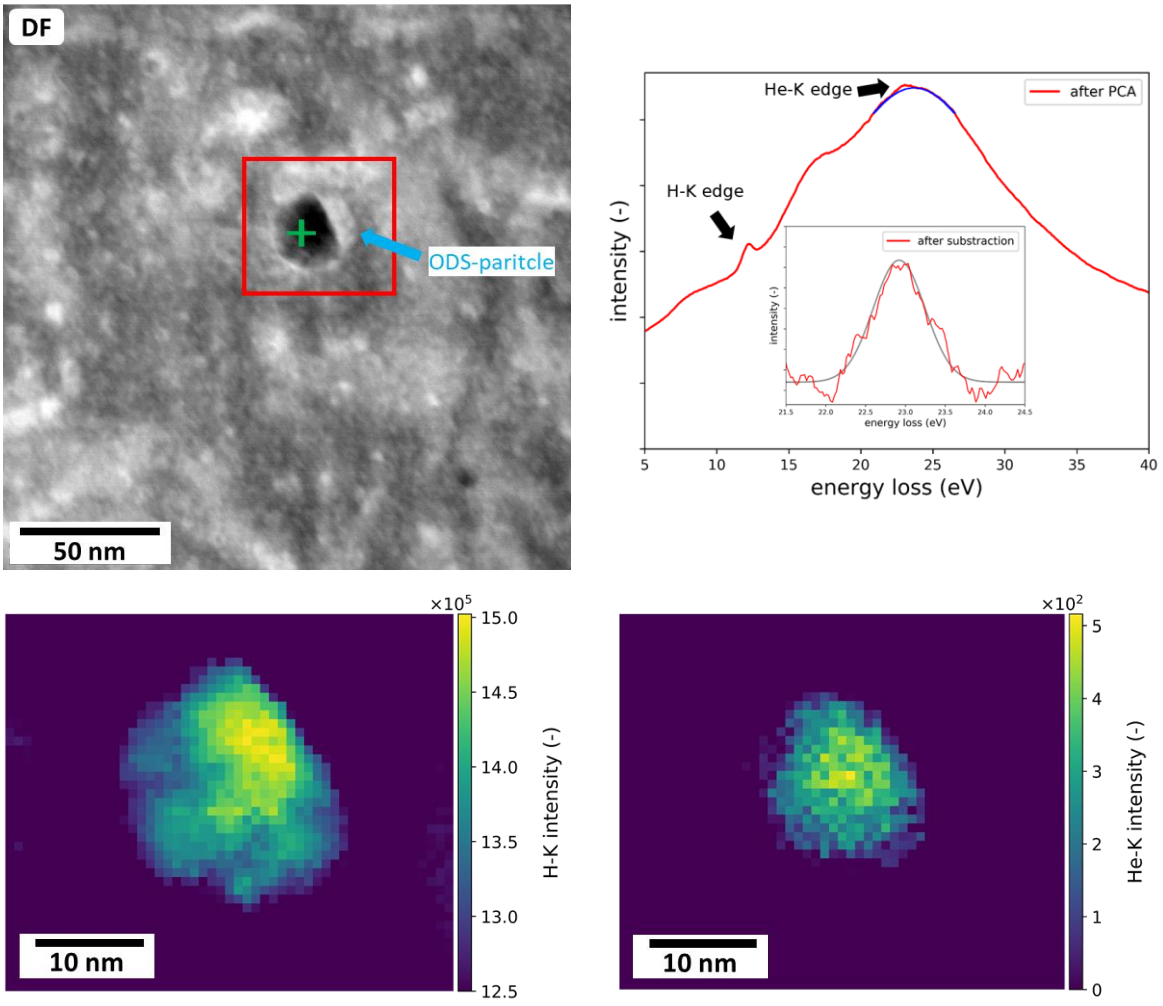

Figure 12: (upper left) STEM-dark field (DF) image of a gas bubble (black) attached to an ODS-particle (grey); (upper right) low loss EELS signal with H-K edge from the bubble inside as indicated by the green cross, the blue line indicates the Gaussian that was used to model the plasmon; (lower left) hydrogen intensity distribution after window integration between 11-14 eV; (lower right) helium intensity distribution after window integration of the residual signal between 22-24 eV

Figure 12 (upper left) shows a scanning transmission electron microscopy (STEM) dark field (DF) image of a gas bubble (black) attached to an ODS-particle (grey) as well as a single low-loss EELS spectrum (upper right) from its interior after principle component analysis (PCA) [26]. The H-K edge is clearly visible at 12.9 eV which is in good accordance with other values reported in the literature [27–29]. The He-K edge, however, is only visible as a small shoulder near the plasmon peak of the metallic matrix around 23 eV. Following Fréchard et al. [30] a Gaussian curve (see blue line in Figure 13 (upper right)) was fitted to the plasmon peak and afterwards subtracted from it to extract the He 1s → 2p peak. The residual signal, which corresponds to the He-K edge, is then also modeled using a Gaussian. To gain insight into the helium and hydrogen distribution, the areas under the two gas-peaks are then simply determined by simple window integration between 21-24 eV and 11-14 eV, respectively. The pixel size for this SI is 9.0 Å. As it can be seen from Figures 13 (lower left) & (lower right) both gases are present throughout the whole bubble. At first glance it looks like, if the helium forms a "core-like" structure within the bubble while the hydrogen resides also further outside in the bubble. More detailed EELS analysis of these materials are in preparation and will be published elsewhere.

4. Discussion

4.1 EUROFER97

At all three irradiation temperatures, bubbles were found both inside and outside the ion implantation region in the EUROFER97 samples. Figures 1, 3 and 4 also show that the largest bubbles were located at a depth of 1.5-2 µm. This observation is in good agreement with the SRIM calculations for this irradiation experiment [19], according to which the helium and hydrogen concentration as well as the displacement damage should have reached its maximum in this area. Apparently, synergetic effects between simultaneous displacement damage as well as helium and hydrogen implantation were observed in this area. In this context, a comparison with the work of Kaiser et al. [31], who irradiated EUROFER97 with Fe^{3+} (3.0 MeV) and He^{+} (1.2 MeV) at 330 °C, 400 °C and 500 °C up to 26 dpa and 450 appm He, and then examined the microstructure in the TEM in the range in which the conditions according to SRIM were exactly effective, is worthwhile. Table 4 shows the results together with the values measured between 1.5 µm and 2 µm.

Table 4: Comparison of dual [31] and triple beam irradiated EUROFER97

	dual beam /triple beam (1.5–2 µm)		
displacement damage (dpa)	26/40		
gas content	450 appm He/500 appm He, 2000 appm H		
temperature (°C)	330/350	400/450	500/550
<d> (nm)	1.3/1.9	1.2/4.8	2.0/4.2
bubble density (10^{22} m^{-3})	20/5.4	9.4/1.5	2.5/1.0
swelling (%)	> 0.02/0.004	> 0.02/0.5	> 0.02/0.1

At all three temperatures, bubbles formed during triple beam irradiation were larger than those formed during dual beam irradiation at comparable temperatures (see Figure 14). The triple beam irradiations at 450 °C and 550 °C led on average even to ~4 times, respectively ~2 times larger bubbles than the dual beam irradiation at 400 °C and 500 °C. Therefore also the swelling

was found to be higher at those temperatures. In contrast, the bubble densities in this work are all lower than for the dual beam irradiation of Kaiser et al.. These observations support the common thesis according to which the presence of hydrogen has a positive influence on bubble growth, but not on bubble formation [32,33]. Wakai et al. [34] came to the same conclusion after dual and triple beam irradiation of F82H. The increased swelling after triple beam irradiation at 470 °C was the result of a comparatively large average bubble diameter. Above the maximum swelling temperature, both the bubble density and the bubble diameter have decreased after the triple beam irradiation. A similar behaviour was found in this work. The comparatively large bubble density at 350 °C reported in this paper can be tentatively explained using the arguments from reference [35], that state that below the maximum swelling temperature, small HeV clusters are stabilized by hydrogen as it increases the binding energy of HeV clusters. At higher temperatures the hydrogen atoms diffuse too fast from the HeV clusters to influence the bubbles. Both, below 400 °C [53] and above 510 °C [58] the swelling in triple beam irradiated FeCr alloy seems to be relatively low. Thus, the influence of hydrogen on the maximum swelling is limited to a temperature window of ~110 °C. It has yet not been conclusively clarified which exact mechanisms are responsible for the synergistic He- and H-effects. Both

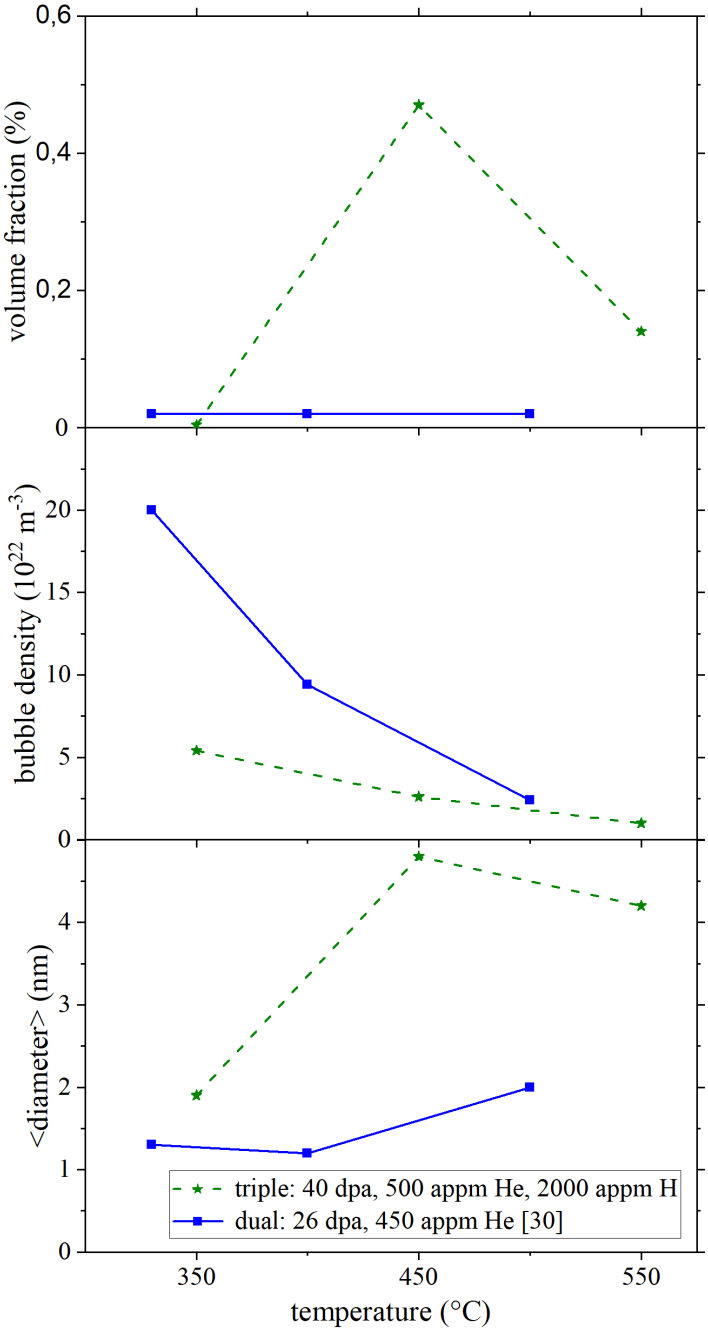

Figure 13: Comparison between dual [30] and triple beam irradiation of EUROFER97

H [36–38] and He [39–41] seem to facilitate the formation of vacancy clusters. Hayward & Deo [42] conclude from their molecular dynamics (MD) simulation, that there is no direct interaction between the two atoms. Instead, they suppose that hydrogen promotes bubble growth by loop punching. Due to the large stress field around a bubble, which is generated by the high pressure in its interior, adjacent matrix atoms can be knocked out of their lattice position. This results in formation Frenkel pairs or dislocation loops [43]. While the created vacancy becomes part of the bubble and increases its volume, the self interstitial atom (SIA) can move freely in the matrix. For the system it is energetically most favorable, if hydrogen is not free in the matrix, but within a He-H-V-Cluster on a vacancy position. The presence of hydrogen causes a reduction of the helium vacancy ratio which is necessary for the energy-minimizing Frenkel pair formation.

Under similar conditions as in the present study, Klimenkov et al. have investigated the microstructure of B-doped EUROFER97 irradiated up to 16.3 dpa and 415 appm He in a high-flux reactor [44]. These samples were used to simulate a fusion relevant helium to dpa ratio under fission neutron irradiation due to enhanced He production by transmutation of boron. The observed bubble structure was significantly coarser than after ion implantation in this work. The cavity density and the maximum bubble diameter were reported to be 0.7 x 10^{22} m^{-3} and 25 nm at 350 °C, at 450 °C 0.8 x 10^{22} m^{-3} and 10 nm. Furthermore, the transition from a homogeneous bubble distribution in the matrix to a heterogeneous bubble formation at dislocations, precipitates and grain boundaries could already be observed at a temperature between 350-450 °C. In addition, the B-doped samples already showed a swelling maximum at 350 °C and not, as observed here, at 450 °C. Thus, these results tend to fit more to the data measured here at 450 °C and 550 °C and it seems there is a temperature shift of ~100 °C between neutron and ion irradiation experiments. In order to simulate the significantly lower damage rates of neutron irradiation [45] higher irradiation temperatures are obviously necessary during ion implantation experiments. The authors in [31,46], who also observed a temperature shift of < 50 °C between neutron and ion irradiation came to the same conclusion.

The observed dependence of the bubble distribution on temperature is in good accordance with the theoretical considerations of Trinkaus & Singh [47] and the bubble growth model of Dethloff [48]. In [48] the author investigated the influence of sinks on bubble development. Grain boundaries were stronger sinks than dislocations under the given conditions. In addition, relatively high temperatures and low helium rates had been shown to promote bubble growth along sinks. The theoretical considerations in [47] connect the bubble diameter and the type of

distribution - homogeneous in the matrix or heterogeneous at microstructural sinks. At 350 °C all bubbles were homogeneously distributed in the matrix and had an average diameter of 1.1 nm. Due to the high supersaturation of the matrix with He ions, two of them can theoretically form a stable nucleus. In addition, the mobility of the implanted helium and the vacancies is limited at this temperature. Thus many centers are available for nucleation of bubbles while diffusion to grain boundaries, dislocations and precipitates but also bubble growth is suppressed. With increasing temperature, larger bubbles with an average diameter of 2.8 nm could be observed at 450 °C. The small He(-vacancy) clusters are no longer thermally stable and the He-atoms are no longer necessarily bound to them as they can diffuse through the material due to the increased temperature. As a result, only clusters that have exceeded a critical size and are stabilized by a sufficiently large supply of He can now grow. Consequently, the bubble density has decreased from 34.9 x 10^{21} m^{-3} to 19.1 x 10^{21} m^{-3}. At 550 °C, the bubbles were no longer distributed exclusively homogeneously in the matrix, but were also found along dislocation lines, precipitates or grain boundaries (see Figure 4 and Figure 5 (left)). The diffusivity of the helium atoms at this temperature was large enough to reach microstructural sinks and anchor there. While the average bubble diameter remained nearly constant, the bubble density decreased to 14.3 x 10^{21} m^{-3}. Accordingly, at this temperature, the implanted helium has attached itself not only in the form of visible bubbles, but also in the form of single atoms or small clusters to sinks which were not visible in the TEM.

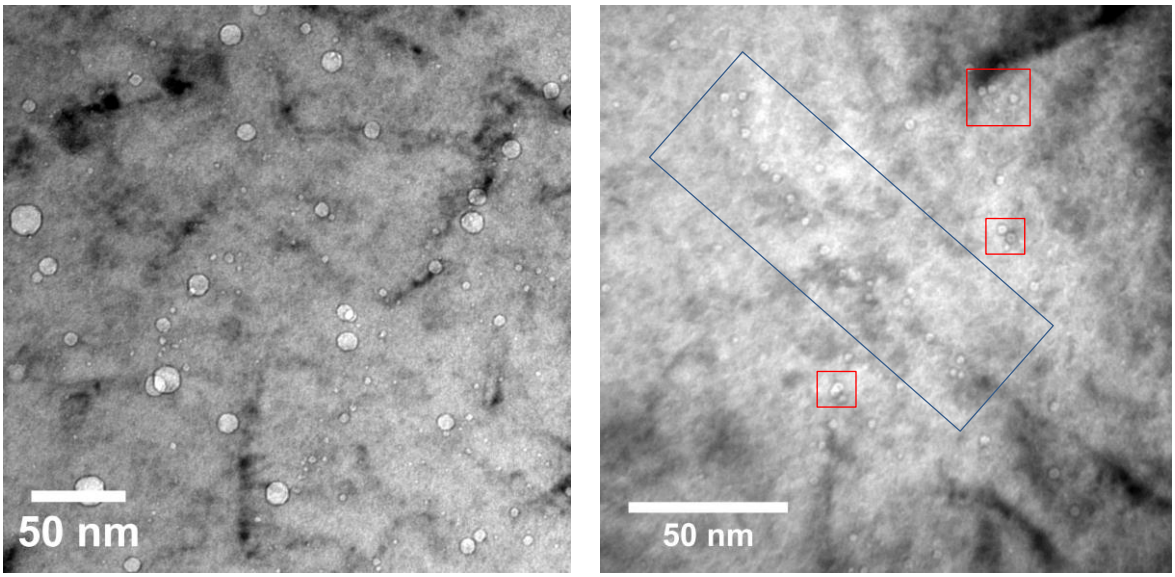

Figure 14: Cluster formation at 450 °C (left) and 550 °C (right) in EUROFER97; the red frames mark bubble coalescence, the blue frame marks bubbles that are attached to a dislocation line.

At 450 °C and 550 °C bubble clusters could be observed repeatedly as exemplified in Figure 15. Larger bubbles were often surrounded by smaller bubbles. In general, bubbles can grow by

two different mechanisms [47,49]. On the one hand by the migration and consolidation of bubbles, on the other hand by Ostwald ripening. The first mechanism assumes, that the bubbles can move due to random rearrangement of the bubble surface by diffusion of the matrix atoms at the surface due to an external driving force, e.g. a stress field or a vacancy concentration gradient. When two bubbles come into contact, they immediately merge together [50]. This mechanism could be the cause of the monomodal particle size distribution at 550 °C (see Figure 16 (lower left)). The Ostwald ripening occurs due to a diffusion flow from smaller to larger bubbles [48] due to different chemical potentials resulting from the different gas pressures of different sized bubbles. Small bubbles dissolve and the released helium atoms are absorbed by larger ones. The more He atoms reside in a bubble, i.e. the larger the pressure in its interior, the larger the energy barrier for diffusing helium atoms to join existing bubbles [51]. Figure 16 shows the size distributions together with the box plots for all three temperatures. The lower end of the box plot is bounded by the 0.25% quantile, the upper end by the 0.75% quantile. The whiskers are limited to 1.5 times the interquartile distance (IQR). At 450 °C, a bimodal bubble distribution was clearly visible. Larger bubbles were always surrounded by the numerically superior smaller ones. Possibly, the bubbles at this temperature have therefore grown by Ostwald ripening.

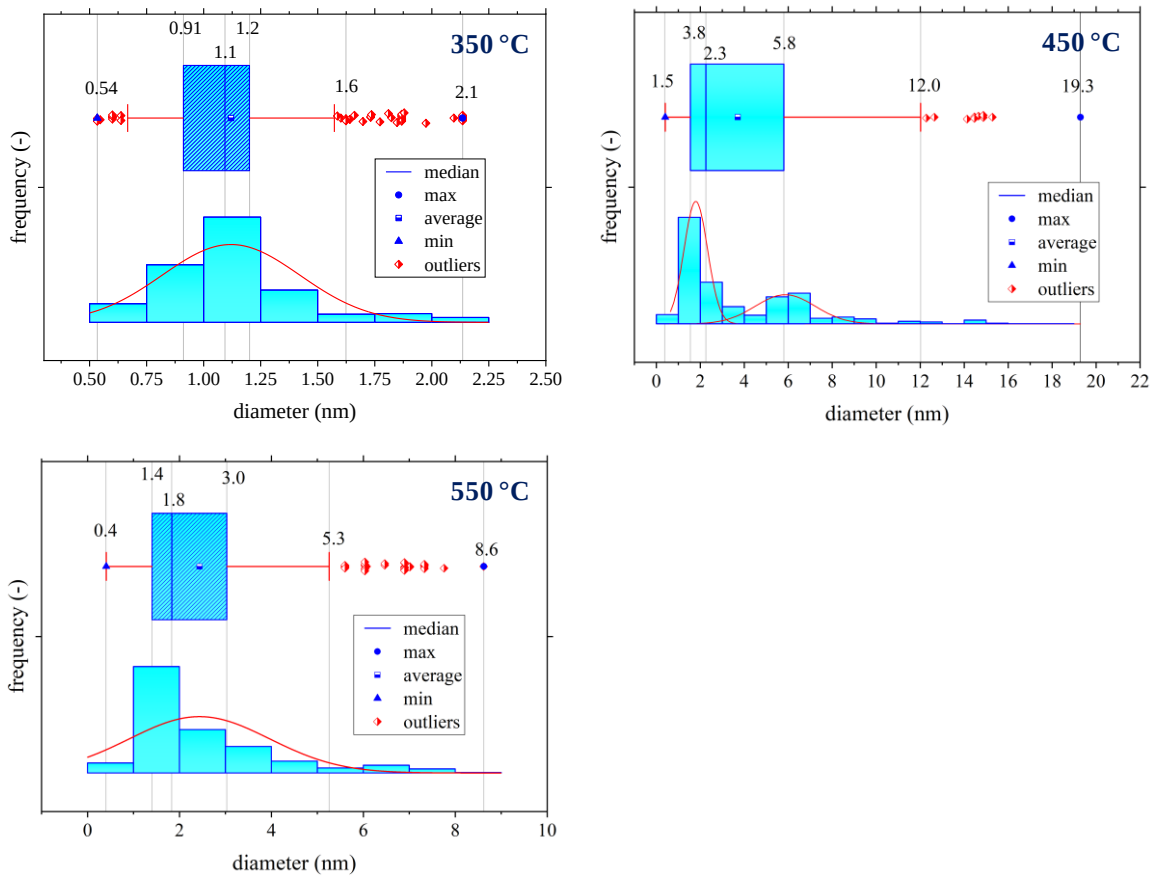

Figure 15: Size distribution of bubbles in EUROFER97 irradiated at (upper left) 350 °C, (upper right) 450 °C, and (lower left) 550 °C. The red curves are the Gaussian fits and the box plot is limited at the lower end by the 0.25 % quantile at the upper end by the 0.75 % quantile. In plot (upper left) the class size is 0.25 nm, in plots (upper right) and (lower left) 1 nm, respectively.

4.2 ODS-EUROFER

Although all three ODS-EUROFER samples were systematically examined in HRTEM, no bubbles could be reliably identified. In earlier studies, ODS-EUROFER samples were irradiated with neutrons [52] or α-particles [5] as well as by multiple ion implantation [46,53]. While bubbles with diameters of up to ~11 nm [5] had clearly formed at the surface of the ODS-particles during the irradiations with α-particles and neutrons, the results of the ion implantations were not completely consistent. Brimbal et al. [46] had irradiated ODS-EUROFER at 400 °C up to 27 dpa, 440 appm He and 2000 appm H and reported bubbles with an average diameter of 2.0 nm and a bubble density of 2.3×10^{22} m^{-3}. However, the bubbles in the pictures presented in this paper - as well as in the present work - cannot be identified without any doubt as such. HRTEM images were not published. Grieveson [53] had investigated ODS-EUROFER irradiated at 300 °C up to 4.5 dpa and 2000 appm He, then analyzed it in HRTEM and could not detect any bubbles. When reviewing TEM images in publications, it should always be noted that these are only snapshots and that it is often difficult to assess bubble formation on the basis of these alone.

In general, under the given conditions in ODS-EUROFER, the formation of bubbles during ion implantation is very limited or non-existent. In this work, either only very small bubbles were formed which could no longer be resolved by the TEM, or the helium is in such a low concentration within the individual grains or at the particle-matrix interfaces that no bubbles were formed.

Assuming that the implanted helium atoms are uniformly attached to all available ODS-particles [15], a helium dose of 500 appm results in a helium concentration of 2.14×10^3 helium-atoms/particle. If one compares the surface of an average oxide particle in ODS-EUROFER, 9.5×10^{-17} m^2 [15], with the area occupied by 2.14×10^3 helium atoms, 3.02×10^{-21} m^2, it quickly becomes clear that a monolayer of helium atoms could have formed around the oxide particles. In addition, a small portion of the helium may have attached itself to other sinks such as grain boundaries or dislocations, thus providing a fine distribution of the implanted helium. Furthermore, helium atoms can also be stored in the lattice gaps of the oxides. Yang et al. [54] calculated the formation energy of substitutional helium with 2.28 eV, for helium within the lowest energy octahedron gap of $Y_2Ti_2O_7$ it was only 0.96 eV.

Accordingly, helium first migrates from the matrix into the ODS-particles or to their interface where it is trapped until a sufficiently large bubble with $r_b > r_c$ has formed at the interface. As soon as the binding energy for helium E_b inside the bubble is lower than the energy E_0 in the oxide, it migrates from the oxide into the attached bubble, which continues to grow due to void absorption. Since the helium atoms interacted mainly with the oxygen anions of the oxides, Yang et al. conclude that all oxides have the potential to capture and store helium. The helium concentrations of 2.14×10^3 helium atoms/particles were obviously not sufficient to form stable bubble nuclei at the surface of the oxides which were large enough to be seen in the TEM.

4.3 13%Cr-ODS steel

As with the EUROFER97 specimens, bubbles were found in the ferritic HIP-ODS at all three irradiation temperatures inside and outside the implantation area. Figures 9, 10 and 12 also show that the largest bubbles, as well as the swelling maxima, were located in the area between 1.5 µm and 2 µm for all samples. Apparently there were also synergetic effects between hydrogen and helium, which promoted the volume increase in this area. It is astonishing, however, that both at 350 °C (4.9 %) and 550 °C (2.5 %) there was an increased swelling, while the volume increase at 450 °C (2.0 %) was comparatively small. At 450 °C and 550 °C the average bubble diameters were increased compared to 350 °C while the bubble densities tended to be lower. Farrell & Lee [55] had justified the synergetic effects between hydrogen and helium with the fact that hydrogen reduces the surface energy of the helium bubbles and thus facilitates the formation of further bubbles. Accordingly, many small bubbles - as can be seen in Figure 10, for example - could have formed at the ODS particles, which later grew into individual large bubbles. However, it is unclear why the swelling has risen again at 550 °C. It is also possible that the synergetic effects between helium and hydrogen in ODS alloys play only a minor role or are decisively influenced by the ODS particles.

The majority of the bubbles have formed on the available Y_2O_3-particles. In other publications [5,56], only between 50 % to 60 % of the helium bubbles were visibly attached to oxide particles and about 40-50 % to other sinks, or they were visible inside the grains. The ferritic ODS-steel was exclusively HIP-treated and should, therefore, have a coarser grain structure than ferritic ODS-steels treated subsequently [57]. The average grain size of the 13%Cr ODS-steel examined here was determined in [15] with 6-8 µm. As a result, there was a strong helium accumulation at the particles. At 350 °C about 70 %, at 450 °C and 550 °C about 60 % of the bubbles were visibly attached to the oxides. As a result, bubbles with diameters of up to 70 nm

were formed at all three temperatures, and even significantly above 107 nm at 350 °C. These observations provide convincing evidence that the oxide particles are strong sinks for helium. However, materials that have been heat after HIPing [8,58,59] show significantly better irradiation behavior. The triple beam irradiation of Fe-14Cr-0.3Y_2O_3 [58] at 600 °C up to ~30 dpa, 500 appm He and 2000 appm H, resulted only in few bubbles with diameters of 2-3 nm. Even after irradiation of the 14%Cr ODS-steel MA957 [60] up to 9 dpa and 380 appm He at 550 °C, only bubbles with diameters of ≤ 1 nm and a bubble density of 3 x 10^2 m^{-3} could be observed. For the present study the densities were 1.3 x 10^{22} m^{-3} and 9.7 x 10^{21} m^{-3} at 450 °C and 550 °C, respectively.

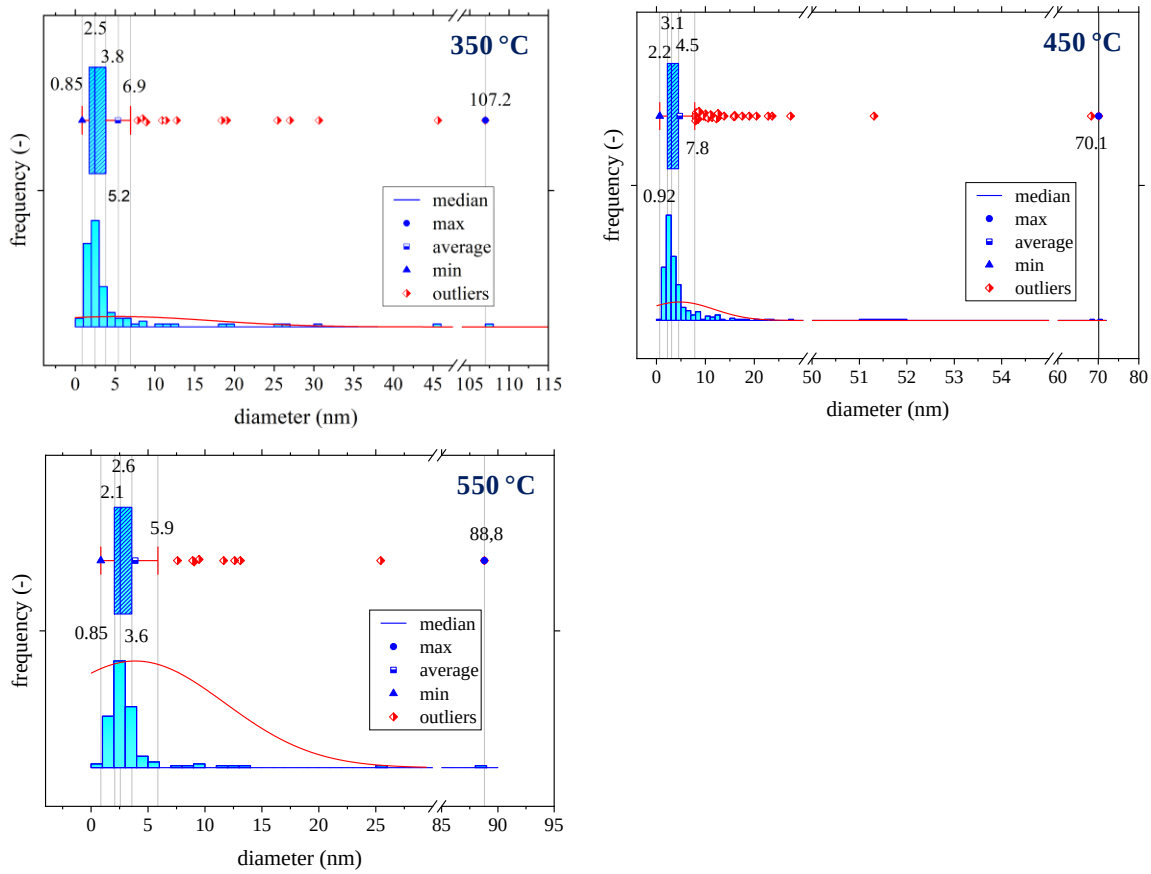

Figure 16: Size distribution of bubbles in the irradiated HIP-ODS (upper left) 350 °C, (upper right) 450 °C, (lower left) 550 °C. The red curves are the Gaussian fit. The box plot is limited at the lower end by the 0.25 % quantile and at the upper end by the 0.75 % quantile. The class size for all three plots is 1 nm.

For the smaller bubbles with a diameter of 3-6 nm, a dependence of the bubble size on the diameter of the ODS particles could be determined. The larger the spherical oxides were, the larger were the bubbles visibly formed on their surface. As already discussed in chapter 4.2, helium can be embedded in the lattice gaps of the oxides or pinned to the particle-matrix interface and later migrate into attached bubbles. Larger oxides can store more helium or trap it at the surface and thus also allow larger bubbles on their surface as bubbles with a higher

helium content can collect more voids until the equilibrium condition $p=2\gamma/r$ is reached. Here p is the pressure, γ the surface energy and r the bubble radius. [8]

Furthermore, the implanted helium was not evenly distributed over a large number of oxide particles, but attached to comparatively few particles in the form of relatively large bubbles. Once a bubble has formed, it also acts as a strong sink for free interstitial helium or HeV clusters. This observation is further illustrated by the size distribution in Figure 17. The box plots are again limited by the 0.25 % or 0.75 % quantile at the lower and upper ends, respectively. The whiskers again mark 1.5 times the IQR.

At all three temperatures, the majority of the bubbles had a diameter between 0.85 nm and 7.8 nm (see Figure 17). In addition, most of the bubbles had a spherical form and were only weakly faceted in some places. In particular, bubbles with diameters > 15 nm were not perfectly spherical. These observations suggest that the pressure inside the bubbles and consequently the helium concentration is relatively high and comparatively few vacancies were necessary for bubble growth.

4.4 Overall Considerations

During our TEM study we could never observe interstitial type defects that could be clearly linked to the ion irradiation. It is well known that at low doses (≤ 1 dpa) or low temperatures (≤ 400 °C) small dislocation loops, often called "black dots", form in Fe-Cr alloys [61–64]. As the sample preparation in our study was done with a FIB it is almost impossible to distinguish between FIB induced damage and ion irradiation defects. With increasing dose or temperature, dislocation loops begin to grow and form extended dislocation networks ([64,65]) (see Figure 5. in [65]). Throughout our TEM investigations we could never localize any dislocation loops that were large enough to be clearly identified as such. At 550 °C, however, we could observe in some places linear arrangements of bubbles (see Figure 4) which seem to be attached to dislocation lines. Therefore it might be concluded that at 350 °C and 450 °C small dislocation loops or black dots could have formed and developed into dislocation structures at 550 °C.

The ODS-EUROFER samples confirmed the outstanding irradiation resistance of this material. Despite intensive investigations, no bubbles could be reliably identified in any of the samples. Apparently, the entire helium was distributed evenly throughout the matrix, at the surface of the ODS-particles or at other microstructural sinks. In contrast, bubble formation in EUROFERR97 occurred already at the lowest irradiation temperature. At 350 °C and 450 °C the bubbles were predominantly freely distributed within the grains. At 550 °C they were also visibly attached to dislocation lines, precipitates and grain boundaries. The HIP-ODS samples reacted worst to the irradiation. Bubbles with diameters up to 107 nm had formed at 350 °C, resulting in local swelling of up to 27 %. The vast majority of the bubbles in this material were attached to the ODS particles at all three irradiation temperatures, at 450 °C and 550 °C partly also to other sinks, especially dislocation lines. An overview of the bubble characteristics is shown in Table 5.

Table 5: Overview of bubble properties in irradiated EUROFER97 and the HIP-PDS irradiated up to 40 dpa, 500 appm He and 2000 appm He.

	EUROFER97			**HIP ODS**		
	350 °C	450 °C	550 °C	350 °C	450 °C	550 °C
bubble density(10^{21} m^{-3})	34.9	19.1	14.3	5.7	13.2	9.7
<diameter> (nm)	1.1	2.8	2.7	5.2	4.7	4.9
max. diameter (nm)	2.1	19.3	8.6	107.2	70.1	88.8
swelling (%)	0.003	0.16	0.03	4.9	2.0	2.5

max. swelling (%)	0.0035	0.47	0.14	27.4	7.0	12.0

For both materials, there may have been synergistic effects between the simultaneous He and H implantation with the superimposed displacement damage. However, the HIP-ODS samples did not show the same temperature dependence as the EUROFER97, where the swelling was highest at 450 °C (see Figure 18), whereas the ferritic ODS-steel already showed strong swelling at 350 °C. At 450 °C, the swelling had then decreased before rising again at 550 °C. Apparently, the ODS particles influenced the bubble formation in such a way that the synergetic effects either played only a minor role or a combined interaction between helium, hydrogen and the ODS particles occurred. Actually, a similar tendency to the EUROFER97 samples was expected. For both materials, however, it could be observed that a comparatively large swelling of the samples is the result of a tendency towards a lower bubble density and a large bubble diameter (see Figure 18). Within the scope of this work, however, it was not possible to conclusively clarify why no visible bubbles were formed in the ODS EUROFER, but bubbles with diameters of up to 107 nm could be seen in the ferritic ODS-steel. Actually, a relatively similar irradiation behavior was expected. Irregularities during irradiation can in principle be ruled out. All samples from this work and the EFDA iron samples from Roldán et al. [21] were irradiated simultaneously in the same experiment. The microstructural investigation of both,

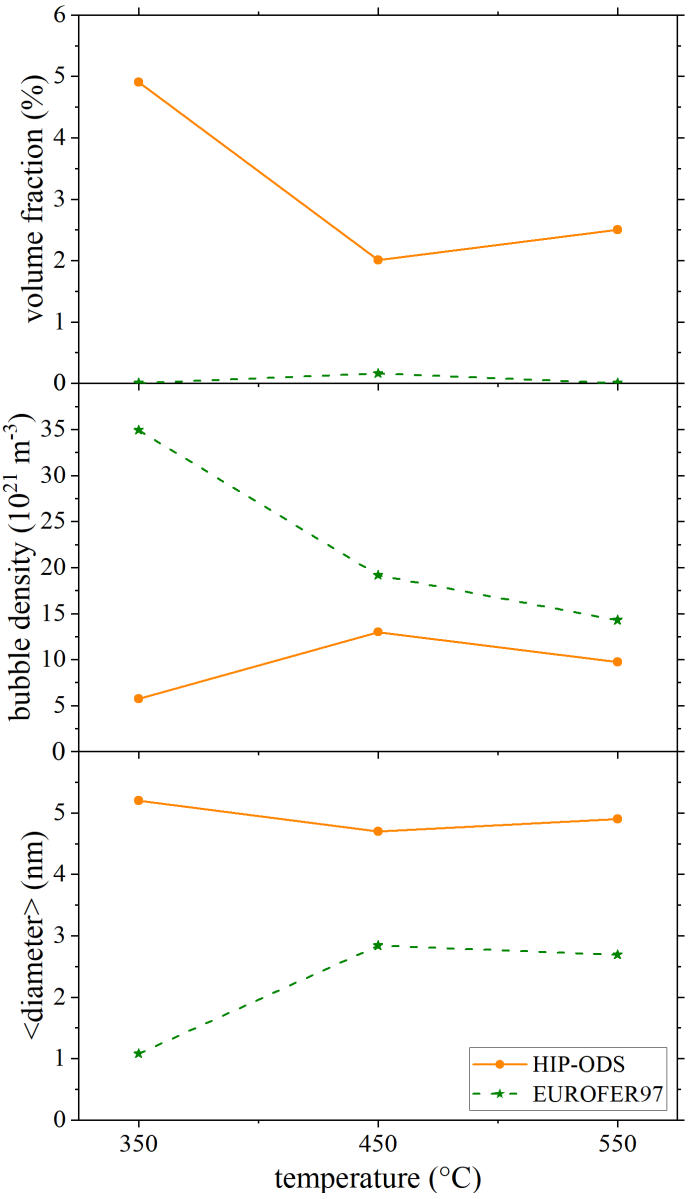

Figure 17: Volume fraction, bubble density and average bubble diameter for the irradiated HIP-ODS and EUROFER97

EUROFER97 and ODS-EUROFER, and of the EFDA iron showed no unexpected changes in the microstructure. Furthermore, the strong difference between the two ODS-steels was observed not only at one but at all three temperatures. Thus the influence of possibly strong local fluctuations of the element concentrations and particle distribution within the individual samples can be excluded. The material properties of the two materials are also relatively similar. Both the mean grain size (4-7 nm vs. 6-8 nm) and the mean size of the oxide particles (10 ± 3 nm vs. 11 ± 6 nm) are of the same order of magnitude for both materials and should therefore also be ruled out as the cause of the strong differences [108]. However, the examination of the non irradiated 13%Cr ODS-steel in the scanning electron microscope (SEM), revealed two possible causes for the deviant irradiation behaviour. Figure 19 (left) shows, on the one hand, that individual grains with a size of up to 10 µm and more could be observed in some places. In these areas (1) there is a smaller number of sinks than in the areas with a finer grain structure (2). Thus, there is a higher tendency for helium to attach to the ODS particles in these regions. On the other hand, pores could be found in some places (see Figure 19 (right)), which indicates an incomplete compaction of the material during HIPing. These cavities may have grown during irradiation to the huge bubbles seen in the TEM due to the influence of temperature, displacement damage and implanted gases. All prepared lamellae had a size of only 6-7 µm. Therefore, it cannot be excluded that the three examined lamellae were randomly cut from those areas of the material where either the grain structure was very coarse or many pores were present. Additionally it is well known that argon, which is used as an inert gas during production, can form small bubbles on top of ODS-particles in non-irradiated material [25,66,67]. These already pre-existing bubbles might have been developed into the observed enormous pores. However, in earlier studies [15] of the non-irradiated material we could never observe these bubbles.

Figure 18 shows that the volume increase in both, HIP-ODS and EUROFER97, are the result of an increased bubble diameter and a comparatively low bubble density respectively. For both materials, the swelling was greatest at all three temperatures at depths between 1.5 µm and 2 µm. However, the EUROFER97 showed a significantly lower swelling (0.16 %) than the HIP-ODS samples, which, due to the strong helium accumulation on the ODS particles at 350°C, are swollen on average by up to 4.9 %. However, the initial porosity was not taken into account. The EUROFER97 samples thus underline the excellent swelling resistance of F/M steels, which usually experience a volume increase of well below 1 %. The ferritic HIP-ODS samples, on the other hand, performed significantly worse than other subsequently treated

ferritic ODS-steels [68,69]. At 350 °C swelling exceeds the 3 % mark, which in some cases is stated in the literature as the embrittlement limit. [7]

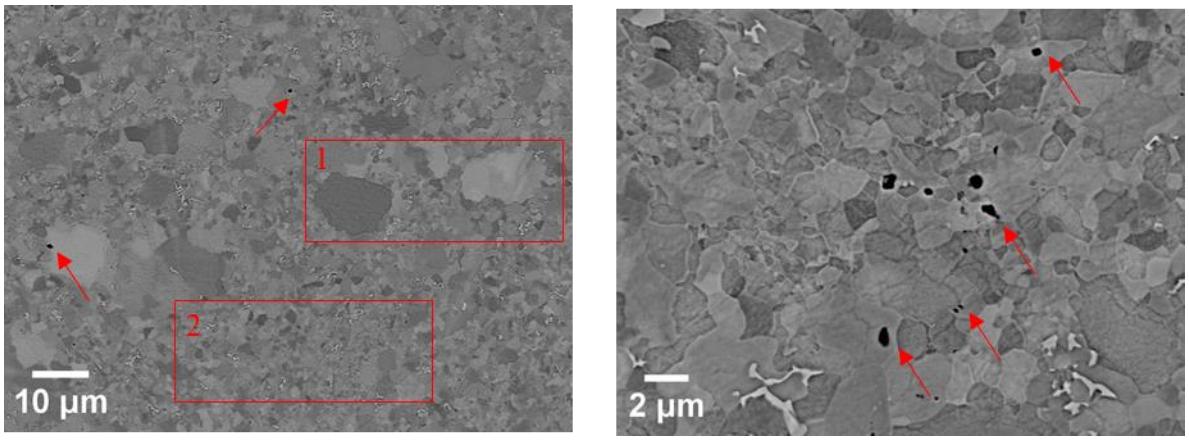

Figure 18: Grain structure of the HIP-ODS in the unirradiated state. The left image shows coarse (1) and fine (2) areas. The red arrows mark small pores which were visible at several places in the material.

5. Concluding Remarks

Within the scope of this work, the gas bubble distribution was analyzed in EUROFER97, ODS-EUROFER and a ferritic 13%Cr ODS-steel, after triple beam irradiation at 350 °C, 450 °C and 550 °C. Both in EUROFER97 and in the ferritic 13%Cr ODS-steel, clearly visible bubbles formed at all three temperatures. Despite extensive investigations, the ODS-EUROFER lamellae showed no bubbles. This underlines the outstanding irradiation resistance of this material. In EUROFER97, bubbles with a size of up to 2.1 nm e were initially homogeneously distributed in the matrix at 350 °C, while bubbles with diameters of up to 19.3 nm, often faceted, were repeatedly observed in the form of small clusters at 450 °C. This indicates bubble growth by Ostwald ripening. After irradiation at 550 °C, a considerable part of the bubbles with a size of up to 8.6 nm could also be localized at dislocations, grain and phase boundaries. The average swelling for this material was highest at 450 °C with 0.16 %.

Comparison of the bubble structure in the EUROFER97 samples from this work with samples irradiated in a high flux reactor suggests a temperature shift of about 100 °C between ion implantation and neutron irradiation.

All samples in which bubbles could be observed showed a maximum bubble size in the range where SRIM calculations suggested helium and hydrogen concentrations and displacement damage to be greatest. Furthermore, the bubble density was comparatively low at the temperatures, which tended to cause a stronger threshold. Thus, synergistic effects between helium and hydrogen should mainly promote bubble growth.

Acknowledgment

The authors are grateful to the JANNuS staff. This work was carried out within the framework of the EUROfusion Consortium and has received funding from the Euratom Research and Training Programme 2014–2018 under grant agreement number 633053. The views and opinions expressed herein do not necessarily reflect those of the European Commission.

Author contributions

V.C, R.V. and P.V. conceived the irradiation experiment, U.J. and M.K. performed the FIB preparation and the TEM investigations, N.Z carried out the optical & statistical analysis of the TEM images as well as the EELS measurements & analysis, P.V provided guidance on result analysis, R.V supervised the irradiation on-site, F.Mota performed the SRIM calculations, N.Z wrote the manuscript with inputs from all authors

Data availability

The raw/processed data required to reproduce these findings cannot be shared at this time as the data also forms part of an ongoing study.

6. References

[1] E. Materna-Morris, A. Möslang, R. Rolli, H.-C. Schneider, Effect of helium on tensile properties and microstructure in 9%Cr–WVTa–steel after neutron irradiation up to 15dpa between 250 and 450°C, Journal of Nuclear Materials 386-388 (2009) 422–425.

[2] J. Knaster, A. Moeslang, T. Muroga, Materials research for fusion, Nat Phys 43 (2016) 424–434.

[3] E. Gaganidze, B. Dafferner, H. Ries, R. Rolli, H.-C. Schneider, J. Aktaa, Irradiation Programme HFR Phase llb - SPICE Impact testing on up to 16.3 dpa irradiated RAFM steels: FZKA 7371, 2008.

[4] E. Gaganidze, C. Petersen, E. Materna-Morris, C. Dethloff, O.J. Weiß, J. Aktaa, A. Povstyanko, A. Fedoseev, O. Makarov, V. Prokhorov, Mechanical properties and TEM examination of RAFM steels irradiated up to 70dpa in BOR-60, Journal of Nuclear Materials 417 (2011) 93–98.

[5] A.I. Ryazanov, O.K. Chugunov, S.M. Ivanov, S.T. Latushkin, R. Lindau, A. Möslang, A.A. Nikitina, K.E. Prikhodko, E.V. Semenov, V.N. Unezhev, P.V. Vladimirov, Tensile properties and microstructure of helium implanted EUROFER ODS, Journal of Nuclear Materials 442 (2013) 153-157.

[6] G.S. Was, Fundamentals of Radiation Materials Science. Metals and Alloys, Springer, 2007.

[7] P. Yvon, M. Le Flem, C. Cabet, J.L. Seran, Structural materials for next generation nuclear systems, Nuclear Engineering and Design 294 (2015) 161–169.

[8] G.R. Odette, M.J. Alinger, B.D. Wirth, Recent Developments in Irradiation-Resistant Steels, Annu. Rev. Mater. Res. 38 (2008) 471–503.

[9] A. Möslang, C. Adelhelm, R. Heidinger, Innovative materials for energy technology, IJMR 99 (2008) 1045–1054.

[10] R.J. Kurtz, G.R. Odette, T. Yamamoto, D.S. Gelles, P. Miao, B.M. Oliver, The transport and fate of helium in martensitic steels at fusion relevant He/dpa ratios and dpa rates, Journal of Nuclear Materials 367-370 (2007) 417–422.

[11] N. Hashimoto, R.L. Klueh, J.P. Robertson, Microstructural Evolution of Ni-doped Ferritic/martensitic Steels Irradiated in the HFIR, MRS Proc. 650 (2000) 748.

[12] E. Wakai, S. Jitsukawa, H. Tomita, K. Furuya, M. Sato, K. Oka, T. Tanaka, F. Takada, T. Yamamoto, Y. Kato, Y. Tayama, K. Shiba, S. Ohnuki, Radiation hardening and -embrittlement due to He production in F82H steel irradiated at 250°C in JMTR, Journal of Nuclear Materials 343 (2005) 285–296.

[13] L. Beck, Y. Serruys, S. Miro, P. Trocellier, E. Bordas, F. Leprêtre, D. Brimbal, T. Loussouarn, H. Martin, S. Vaubaillon, S. Pellegrino, D. Bachiller-Perea, Ion irradiation and radiation effect characterization at the JANNUS-Saclay triple beam facility, J. Mater. Res. 30 (2015) 1183–1194.

[14] E. Gaganidze, H.-C. Schneider, B. Dafferner, J. Aktaa, High-dose neutron irradiation embrittlement of RAFM steels, Journal of Nuclear Materials 355 (2006) 83–88.

[15] S. Rogozhkin, A. Bogachev, O. Korchuganova, A. Nikitin, N. Orlov, A. Aleev, A. Zaluzhnyi, M. Kozodaev, T. Kulevoy, B. Chalykh, R. Lindau, J. Hoffmann, A. Möslang, P. Vladimirov, M. Klimenkov, M. Heilmaier, J. Wagner, S. Seils, Nanostructure evolution in ODS steels under ion irradiation, Nuclear Materials and Energy 9 (2016) 66–74.

[16] Nuclear Fusion Programme | Annual Report of the Association Karlsruhe Institute of Technology KIT/EURATOM | January 2012 - December 2012, 2012.

[17] R. Lindau, A. Möslang, M. Rieth, M. Klimiankou, E. Materna-Morris, A. Alamo, A.-A.F. Tavassoli, C. Cayron, A.-M. Lancha, P. Fernandez, N. Baluc, R. Schäublin, E. Diegele, G. Filacchioni, J.W. Rensman, B.v.d. Schaaf, E. Lucon, W. Dietz, Present development status of EUROFER and ODS-EUROFER for application in blanket concepts, Fusion Engineering and Design 75-79 (2005) 989–996.

[18] J.F. Ziegler, http://www.srim.org/, 2017, accessed 23 August 2017.

[19] M. Roldán, P. Fernández, R. Vila, A. Gómez-Herrero, F.J. Sánchez, The effect of triple ion beam irradiation on cavity formation on pure EFDA iron, Journal of Nuclear Materials 479 (2016) 100–111.

[20] D.B. Williams, C.B. Carter, Transmission electron microscopy: A textbook for materials science, 2nd ed., Springer, New York, 2008.

[21] M.L. Jenkins, Characterisation of radiation-damage microstructures by TEM, Journal of Nuclear Materials 216 (1994) 124–156.

[22] J. Schindelin, I. Arganda-Carreras, E. Frise, V. Kaynig, M. Longair, T. Pietzsch, S. Preibisch, C. Rueden, S. Saalfeld, B. Schmid, J.-Y. Tinevez, D.J. White, V. Hartenstein, K. Eliceiri, P. Tomancak, A. Cardona, Fiji: an open-source platform for biological-image analysis, Nature methods 9 (2012) 676–682.

[23] Standard Practice for Measurement of Mechanical Properties During Charged-Particle Irradiation, ASTM International, 2016.

[24] R.F. Egerton, Electron Energy-Loss Spectroscopy in the Electron Microscope, 1986.

[25] M. Klimenkov, Quantitative measurement of argon inside of nano-sized bubbles in ODS steels, Journal of Nuclear Materials 411 (2011) 160–162.

[26] S. Wold, K. Esbensen, P. Geladi, Principal component analysis, Chemometrics and Intelligent Laboratory Systems 2 (1987) 37–52.

[27] M.S. Blackmur, S. Dumbill, I. MacLaren, D. Hernandez-Maldonado, P.D. Styman, M. Gass, R.J. Nicholls, J.M. Hyde, Q.M. Ramasse, K.J. Annand, J.S. Smith, N. Gotham, The association of hydrogen with nanometre bubbles of helium implanted into zirconium, Scripta Materialia 152 (2018) 102–106.

[28] M. Klimenkov, P. Vladimirov, J. Hoffmann, N. Zimber, A. Möslang, V. Kuksenko, First simultaneous detection of helium and tritium inside bubbles in beryllium, Micron (Oxford, England 1993) 127 (2019) 102754.

[29] Y. Lu, W.-J. Yin, K.-L. Peng, K. Wang, Q. Hu, A. Selloni, F.-R. Chen, L.-M. Liu, M.-L. Sui, Self-hydrogenated shell promoting photocatalytic H2 evolution on anatase TiO2, Nature communications 9 (2018) 2752.

[30] S. Fréchard, M. Walls, M. Kociak, J.P. Chevalier, J. Henry, D. Gorse, Study by EELS of helium bubbles in a martensitic steel, Journal of Nuclear Materials 393 (2009) 102–107.

[31] B. Kaiser, C. Dethloff, E. Gaganidze, D. Brimbal, M. Payet, P. Trocellier, L. Beck, J. Aktaa, TEM study and modeling of bubble formation in dual-beam He+/Fe3+ ion irradiated EUROFER97, Journal of Nuclear Materials 484 (2017) 59–67.

[32] J. Marian, T. Hoang, M. Fluss, L.L. Hsiung, A review of helium–hydrogen synergistic effects in radiation damage observed in fusion energy steels and an interaction model to guide future understanding, Journal of Nuclear Materials 462 (2015) 409–421.

[33] T. Tanaka, K. Oka, S. Ohnuki, S. Yamashita, T. Suda, S. Watanabe, E. Wakai, Synergistic effect of helium and hydrogen for defect evolution under multi-ion irradiation of Fe–Cr ferritic alloys, Journal of Nuclear Materials 329-333 (2004) 294–298.

[34] E. Wakai, M. Ando, T. Sawai, S. Ohnuki, Effect of Helium and Hydrogen Production on Irradiation Hardening of F82H Steel Irradiated by Ion Beams, Mater. Trans. 48 (2007) 1427–1430.

[35] E. Wakai, T. Sawai, K. Furuya, A. Naito, T. Aruga, K. Kikuchi, S. Yamashita, S. Ohnuki, S. Yamamoto, H. Naramoto, S. Jistukawa, Effect of triple ion beams in ferritic/martensitic steel on swelling behavior, Journal of Nuclear Materials 307-311 (2002) 278–282.

[36] E. Hayward, C.-C. Fu, Interplay between hydrogen and vacancies in \alpha-Fe, Phys. Rev. B 87 (2013) 174103.

[37] B. Irigoyen, R. Ferullo, N. Castellani, A. Juan, The interaction of hydrogen with an Fe vacancy, Journal of Physics D: Applied Physics 29 (1996) 1306.

[38] E. Hayward, C. Deo, Energetics of small hydrogen-vacancy clusters in bcc iron, Journal of physics. Condensed matter an Institute of Physics journal 23 (2011) 425402.

[39] G. Lucas, R. Schäublin, Stability of helium bubbles in alpha-iron, Journal of Nuclear Materials 386-388 (2009) 360–362.

[40] K. Morishita, R. Sugano, B.D. Wirth, MD and KMC modeling of the growth and shrinkage mechanisms of helium–vacancy clusters in Fe, Journal of Nuclear Materials 323 (2003) 243–250.

[41] K. Morishita, R. Sugano, B.D. Wirth, T. La Diaz de Rubia, Thermal stability of helium–vacancy clusters in iron, Nuclear Instruments and Methods in Physics Research Section B: Beam Interactions with Materials and Atoms 202 (2003) 76–81.

[42] E. Hayward, C. Deo, Synergistic effects in hydrogen-helium bubbles, Journal of physics. Condensed matter an Institute of Physics journal 24 (2012) 265402.

[43] N. Gao, H. van Swygenhoven, M. Victoria, J. Chen, Formation of dislocation loops during He clustering in bcc Fe, Journal of physics. Condensed matter an Institute of Physics journal 23 (2011) 442201.

[44] M. Klimenkov, A. Möslang, E. Materna-Morris, Helium influence on the microstructure and swelling of 9%Cr ferritic steel after neutron irradiation to 16.3dpa, Journal of Nuclear Materials 453 (2014) 54–59.

[45] C. Dethloff, E. Gaganidze, V.V. Svetukhin, J. Aktaa, Modeling of helium bubble nucleation and growth in neutron irradiated boron doped RAFM steels, Journal of Nuclear Materials 426 (2012) 287–297.

[46] D. Brimbal, L. Beck, O. Troeber, E. Gaganidze, P. Trocellier, J. Aktaa, R. Lindau, Microstructural characterization of Eurofer-97 and Eurofer-ODS steels before and after multi-beam ion irradiations at JANNUS Saclay facility, Journal of Nuclear Materials 465 (2015) 236–244.

[47] H. Trinkaus, B.N. Singh, Helium accumulation in metals during irradiation – where do we stand?, Journal of Nuclear Materials 323 (2003) 229–242.

[48] C. Dethloff, Modeling of helium bubble nucleation and growth in neutron irradiated RAFM steels. Dissertation, KIT Scientific Publishing; Technische Informationsbibliothek u. Universitätsbibliothek, Karlsruhe, 2012.

[49] H. Trinkaus, H. Ullmaier, A model for the high-temperature embrittlement of metals containing helium, Philosophical Magazine A 39 (1979) 563–580.

[50] E.E. Gruber, Calculated Size Distributions for Gas Bubble Migration and Coalescence in Solids, Journal of Applied Physics 38 (1967) 243–250.

[51] X. Gai, T. Lazauskas, R. Smith, S.D. Kenny, Helium bubbles in bcc Fe and their interactions with irradiation, Journal of Nuclear Materials 462 (2015) 382–390.

[52] M. Klimenkov, R. Lindau, U. Jäntsch, A. Möslang, Effect of irradiation temperature on microstructure of ferritic-martensitic ODS steel, Journal of Nuclear Materials 493 (2017) 426–435.

[53] E.M. Grieveson, Irradiation Effectos on the Deformation of Oxide Dispersion Strengthened Steels. Dissertation, 2015.

[54] L. Yang, Y. Jiang, G. Robert Odette, T. Yamamoto, Z. Liu, Y. Liu, Trapping helium in Y2Ti2O7 compared to in matrix iron: A first principles study, Journal of Applied Physics 115 (2014) 143508.

[55] K. Farrell, E.H. Lee, Ion Damage in a Fe-10Cr-6Mo-0.5Nb Ferritic Steel, in: A.S. Kumar, F.A. Garner, N.H. Packan (Eds.), Radiation-induced changes in microstructure: 13th international symposium (part I), American Society for Testing and Materials, Philadelphia, Pa, 1987, 498-498-10.

[56] P.D. Edmondson, C.M. Parish, Y. Zhang, A. Hallén, M.K. Miller, Helium bubble distributions in a nanostructured ferritic alloy, Journal of Nuclear Materials 434 (2013) 210–216.

[57] C.C. Eiselt, Eigenschaftsoptimierung der nanoskaligen ferritischen ODS-Legierung 13Cr-1W-0,3Y_2O_3-0,3TiH_2, metallkundliche Charakterisierung und Bestimmung von Struktur-Eigenschaftskorrelationen. Dissertation, 2010.

[58] M. Šćepanović, V. de Castro, T. Leguey, M.A. Auger, S. Lozano-Perez, R. Pareja, Microstructural stability of ODS Fe–14Cr (–2W–0.3Ti) steels after simultaneous triple irradiation, Nuclear Materials and Energy 9 (2016) 490–495.

[59] G.R. Odette, Recent Progress in Developing and Qualifying Nanostructured Ferritic Alloys for Advanced Fission and Fusion Applications, JOM 66 (2014) 2427–2441.

[60] T. Yamamoto, G.R. Odette, P. Miao, D.T. Hoelzer, J. Bentley, N. Hashimoto, H. Tanigawa, R.J. Kurtz, The transport and fate of helium in nanostructured ferritic alloys at fusion relevant He/dpa ratios and dpa rates, Journal of Nuclear Materials 367-370 (2007) 399–410.

[61] K. Arakawa, M. Hatanaka, H. Mori, K. Ono, Effects of chromium on the one-dimensional motion of interstitial-type dislocation loops in iron, Journal of Nuclear Materials 329-333 (2004) 1194–1198.

[62] Z. Yao, M. Hernández-Mayoral, M.L. Jenkins, M.A. Kirk, Heavy-ion irradiations of Fe and Fe–Cr model alloys Part 1: Damage evolution in thin-foils at lower doses, Philosophical Magazine 88 (2008) 2851–2880.

[63] J. Chen, P. Jung, W. Hoffelner, H. Ullmaier, Dislocation loops and bubbles in oxide dispersion strengthened ferritic steel after helium implantation under stress, Acta Materialia 56 (2008) 250–258.

[64] M. Klimenkov, U. Jäntsch, M. Rieth, A. Möslang, Correlation of microstructural and mechanical properties of neutron irradiated EUROFER97 steel, Journal of Nuclear Materials - under review (2020).

[65] P.M. Derlet, S.L. Dudarev, Microscopic structure of a heavily irradiated material, Phys. Rev. Materials 4 (2020) 582.

[66] J. Hoffmann, Ferritische ODS-Stähle - Herstellung, Umformung und Strukturanalyse. Dissertation, 2013.

[67] M. Klimiankou, R. Lindau, A. Möslang, Energy-filtered TEM imaging and EELS study of ODS particles and argon-filled cavities in ferritic-martensitic steels, Micron (Oxford, England 1993) 36 (2005) 1–8.

[68] M.B. Toloczko, D.S. Gelles, F.A. Garner, R.J. Kurtz, K. Abe, Irradiation creep and swelling from 400 to 600 °C of the oxide dispersion strengthened ferritic alloy MA957, Journal of Nuclear Materials 329-333 (2004) 352–355.

[69] P. Dubuisson, R. Schill, M. Hugon, I. Grislin, J. Séran, Behavior of an Oxide Dispersion Strengthened Ferritic Steel Irradiated in Phenix, West Conshohocken, PA, 1999.

[70] N.N. Greenwood, A. Earnshaw, Chemistry of the elements, 2nd ed., Butterworth-Heinemann, Oxford u.a., 1997.

7. Appendix

Calculation of He density at ODS-particles

atomic radius iron:	126 pm = 1.26 x 10^{-10} m [70]
atomic radius helium	31 pm = 0.31 x 10^{-10} m [70]
oxide particle density:	1.9 x 10^{22} m^{-3} [15]
<oxid particle size>	5.5 nm [15]

volume of a cubic face centered (fcc) unit cell

$V = a^3$ with $a = \frac{4r}{\sqrt{3}}$

$$a = \frac{4 \text{ x } 1.26 \text{ x } 10^{-10} \text{ m}}{\sqrt{3}} = 2.91 \text{ x } 10^{-10} \text{ m}$$

$$V = 2.46 \text{ x } 10^{-29} \text{ m}^3$$

unit cells/m^3:

$$\frac{1 \text{ unit cell}}{2.46 \text{ x } 10^{-29} \text{ m}^3} = 4.07 \text{ x } 10^{28} \frac{\text{unit cells}}{\text{m}^3}$$

With 2 atoms per cubic fcc unit cell the number of atoms/m^3 is given as:

$$2 \text{ atoms x } 4.07 \text{ x } 10^{28} \text{ m}^{-3} = 8.13 \text{ x } 10^{28} \frac{\text{atoms}}{\text{m}^3}$$

helium atoms/m^3:

$$500 \text{ appm He x } 8.13 \text{ x } 10^{28} \frac{\text{helium atoms}}{\text{m}^3} = 4.07 \text{ x } 10^{25} \frac{\text{helium atoms}}{\text{m}^3}$$

helium atoms/particle:

$$\frac{4.07 \text{ x } 10^{25} \frac{\text{helium atoms}}{\text{m}^3}}{1.9 \text{ x } 10^{22} \frac{\text{particle}}{\text{m}^3}} = 2.14 \text{ x } 10^{3} \frac{\text{helium atoms}}{\text{particle}}$$

surface of an ODS-particle:

$A = 4\pi r^2 = 4\pi \text{ x } (2.75 \text{ x } 10^{-9}\text{m})^2 = 9.5 \text{ x } 10^{-17} \text{ m}^2$

Surface of 2.14 x 10^3 helium atoms:

$A = 2.14 \text{ x } 10^3 \text{ x } 2\pi r^2 = 2.14 \text{ x } 10^3 \text{ x } 2\pi \text{ x } (0.31 \text{ x } 10^{22})^2 = 3.02 \text{ x } 10^{-21} \text{ m}^2$